공학박사학위논문

Protease Activatable Peptide Depot for Photodynamic Therapy and Riboflavin-Induced Hyaluronic acid/Peptide Hydrogel for Bio-Applications

단백질 분해효소에 의한 활성화 펩타이드 디포를 이용한 광역동 치료 및 리보플라빈에 의한 히알루론산/펩타이드 하이드로젤의 생물의학적 응용

2018년 2월

서울대학교 대학원

화학생물공학부

박 성 준

Protease Activatable Peptide Depot for Photodynamic Therapy and Riboflavin-Induced Hyaluronic acid/Peptide Hydrogel for Bio-Applications

단백질 분해효소에 의한 활성화 펩타이드 디포를 이용한 광역동 치료 및 리보플라빈에 의한 히알루론산/펩타이드 하이드로겔의 생물의학적 응용

지도 교수 이 윤 식

이 논문을 공학박사학위논문으로 제출함
2018년 2월
서울대학교 대학원
화학생물공학부
박 성 준

박성준의 공학박사학위논문을 인준함
2017년 7월

위 원 장 김 병 기 (인)

부위원장 이 윤 식 (인)

위 원 한 지 숙 (인)

위 원 김 세 훈 (인)

위 원 신 동 식 (인)

ABSTRACT

Protease Activatable Peptide Depot for Photodynamic Therapy and Riboflavin-Induced Hyaluronic acid/Peptide Hydrogel for Bio-Applications

Sung Jun Park

School of Chemical and Biological Engineering

The Graduate School

Seoul National University

Peptides are widely studied in various biological applications because of their natural origins, biocompatibility, and diverse functions. One of the most common researches performed using peptides is associated with drug delivery to cancer. These include various functional peptides such as RGD or MMP-7, which are related to overexpressed factors concerning cancer. Recently, structural features of peptides are gaining great interest, where delicate organization could be achieved by specifically designed sequences. These peptides could

be utilized in the fabrication of various biomaterials such as hydrogels.

In chapter 1, a cyclic internalizing RGD peptide (iRGD) derivative (Ppa-iRGDC-BK01) that self-aggregates into a molecular depot was applied to photodynamic therapy (PDT). Ppa-iRGDC-BK01 is designed as an in-situ self-implantable photosensitizer so that it forms depot by itself upon injection, and its molecular activities (cancer cell internalization and photosensitization) are activated by sustained release and tumor-selective proteolytic/reductive cleavage of the iRGD segment. It turned out that the self-aggregation of Ppa-iRGDC-BK01 into depot exerts a multiple-quenching effect to effectively prevent nonspecific phototoxicity and photobleaching, while allowing for its sustained release, tumor accumulation and tumoral activation of photosensitivity over time. Such a single-component photosensitizing molecular depot approach, combined with a strategy of tumor-targeted therapeutic activation, opens up a new way to safer and more precise repetition of PDT through single injection and multiple irradiations.

In chapter 2, Tyramine conjugated hyaluronic acid (HA-Ty) was rheometrically modulated with tyrosine rich peptides (TRP) in hydrogel formation, and its potential as a wound healing agent was tested. Riboflavin-sensitized photo-crosslinking was utilized as a gelation strategy, where riboflavin induces covalent linkages between the phenolic groups of conjugated tyramines under UV irradiation.

TRP, as an additive, enhanced the storage modulus of the HA-Ty hydrogel because the tyrosine residues could also participate in the crosslinking with the phenol moieties of the HA-Ty. The HA-Ty/TRP hybrid hydrogels were tested as a plausible healing agent for wound injuries.

Keywords: Photodynamic therapy, Internalizing RGD (iRGD), Activatable photosensitizer, Subcutaneous depot, Sustained release, Hyaluronic acid hydrogel, Tyrosine-rich peptides, Riboflavin, Photo-crosslinking, Wound healing

Student number: 2014-30250

TABLE OF CONTENTS

LIST OF SCHEMES

LIST OF FIGURES

LIST OF ABBREVIATIONS

BK01	Black-01
CCK8	Cell Counting Kit 8
ConC	Cyclic Cys-Gly-Gly-Gly-Gly-Gly-Pro-Asp-Cys
DAPI	4',6-diamidino-2-phenylindole
DIPEA	N,N-diisopropylethylamine
DMF	Dimethylformamide
DMSO	Dimethyl sulfoxide
DTT	Dithiothreitol
EDC	Ethyl(dimethylaminopropyl) carbodiimide
EtOH	Ethyl alcohol
FBS	Fetal bovine serum
FRET	Förster resonance energy transfer
GHK-Cu	Gly-His-Lys-Copper
HA	Hyaluronic acid
HA-Ty	Tyramine-conjugated hyaluronic acid
HPLC	High performance liquid chromatography
HRMS	High resolution mass spectrometer
iRGD	Cyclic Cys-Arg-Gly-Asp-Arg-Gly-Pro-Asp-Cys
MALDI/TOF	Matrix-assisted laser desorption/ionization time-of-flight mass spectrometer
MMP-7	Matrix metalloproteinase-7
MTT	3-(4,5-Dimethylthiazol-2-yl)-2,5-Diphenyltetrazolium Bromide
NHS	N-hydroxysuccinimide
NMR	Nuclear magnetic resonance
NRP-1	Neuropilin-1
PBS	Phosphate buffer saline
PDT	Photodynamic Therapy
PS	Photosensitizer

Ppa	Pyropheophorbide-*a*
RGD	Arg-Gly-Asp
RNO	*p*-nitrosodimethylaniline
ROI	Region of interest
ROS	Reactive oxygen species
RPMI	Roswell Park Memorial Institute
SOG	Singlet oxygen generation
TCSPC	Time correlated single photon counting
TFA	Trifluoroacetic acid
TRP	Tyrosine rich peptide
U-87 MG	Human primary glioblastoma
UVA	Ultraviolet A

Introduction

1. Peptide linkers

Naturally existing multi-domain proteins are composed of two or more functional domains joined together by peptide linkers.[1] These linker peptides not only serve to connect the protein moieties, but also provide other functions such as maintaining cooperative inter-domain interactions, or preserving biological activity.[2,3] Knowledge of natural peptide linkers in multi-domain proteins gives helpful information in designing empirical linkers in recombinant fusion proteins. Empirical linkers are classified into 3 categories which are flexible, rigid, and cleavable linkers (Fig. 1).

Flexible linkers are used when the joined domains require a certain degree of movement.[4] Usually small, non-polar (e.g. Gly), or polar (e.g. Ser, Thr) amino acids are involved in this category. The small sizes of these amino acids allow flexibility and mobility of connected moieties. While mobility is given by flexible linkers, lack of rigidity could lead to poor expression yields or loss of function. Rigid linkers could supplement these limitations by providing fixed distance between domains.

Examples of rigid linkers include alpha helix-forming $(EAAAK)_n$, and Proline-rich $(XP)_n$ with X preferably Ala, Lys, or Glu.[5,6] At last, *in vivo* cleavable linkers are introduced under the circumstances where free functional domains need to be released in biological environments.[7] Flexible or rigid linkers are usually stable peptides that will not be preferentially cleaved *in vivo*, and this could lead to steric hindrance between domains, decreased bioactivity, or altered biodistribution and metabolism of the protein moieties. One of the most studied cleavable linkers is the utilization of disulfide linkage, which could be reduced by natural reductive agents such as glutathione.[8] In a similar manner, cleavage of the linkers could be carried out by various proteases that are expressed under pathological conditions. These proteases include matrix metalloproteinase (MMP), caspase, serine protease, etc.[9]

Linker		Advantages	Characteristics	Examples
Flexible	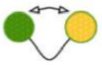 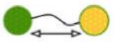	Allow for interaction between domains, or Increase spatial separation between domains	Rich in small or hydrophilic amino acids	$(GGGGS)_n$, $(G)_n$
Rigid		Maintain distance between domains	Helical structure or rich in Pro	$(EAAAK)_n$, $(XP)_n$
Cleavable		Allow for *in vivo* separation of domains	Reductive or enzymatic cleavage	Disulfide, protease sensitive sequences

Figure 1. Three categories of peptide linkers that exist in protein fusion technology.

2. Application of peptide linkers in biological probes

Among the categorized peptide linkers, protease cleavable peptides are widely chosen in various biological applications because of their biocompatibility and high functionality. MMP has long been of interest as pharmaceutical targets because it could be a marker molecule in various types of diseases.[10-13] MMP-2/9 are related with cancer, MMP-7 with atherosclerosis, and MMP-13 with rheumatoid arthritis.[14] In a previous research, a peptide sequence GPLGLAG as a MMP-2-cleavable linker was used to combine a photosensitizer (PS) and a cell penetrating peptide (CPP) to make a photodynamic therapy (PDT) agent (Fig. 2A).[15] This particular PDT agent was designed to control the probe's activity by linking a counteracting polyanionic peptide (E_8) to the polycationic CPP (R_9) with the MMP-2 substrate. Cleavage would occur near the tumor with excess MMP-2 and then the CPP could guide the probe into the cells. Then, the probe could act as an active PS to be applied to photodynamic therapy.

Another example of protease cleavable linker probe is the utilization of caspase-3 targeted peptide substrate (Fig. 2B). Caspase-3 is one of the directly related proteases in the process of apoptosis.[16-18] Apoptosis, a programmed cell death is initiated in majority of anticancer therapies, so detecting the progression of apoptosis could clinically assist determining therapeutical conditions. Bullok *et al*. developed a caspase-activatable, cell permeable peptide probe to image apoptosis in cell culture and *in vivo*.[19] Peptide substrate DEVD was used as a linker together with a Tat-peptide-based cell permeation sequence. Alexa fluorophore and a quencher was used for controlled imaging, where caspase cleavage of DEVD would trigger the fluorescence activation. The results showed amplified signals in doxorubicin treated apoptotic cells, and parasite-induced apoptosis was also detected in human colon xenograft mouse models.

A

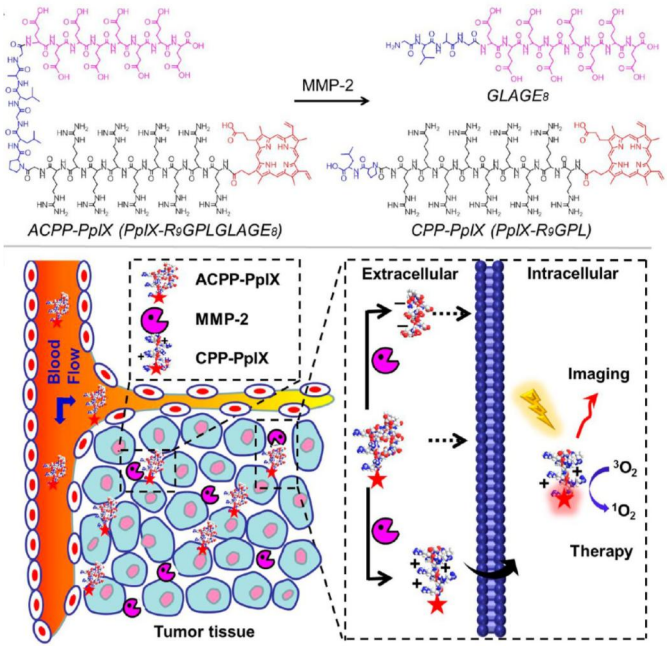
MMP-2
GLAGE8
ACPP-PpIX (PpIX-R8GPLGLAGE8)
CPP-PpIX (PpIX-R8GPL)
ACPP-PpIX
MMP-2
CPP-PpIX
Blood Flow
Tumor tissue
Extracellular
Intracellular
Imaging
Therapy
$^3O_2$
$^1O_2$

B

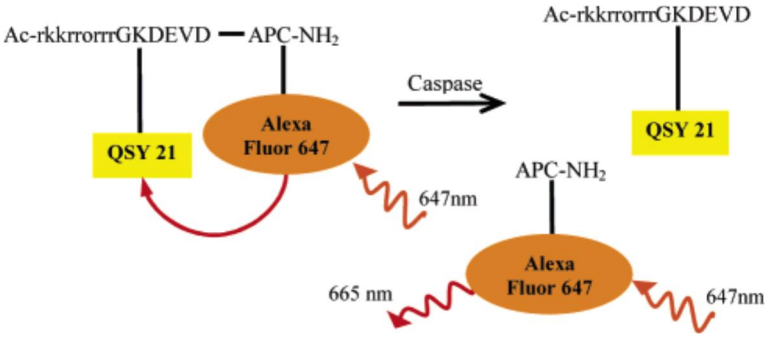
Ac-rkkrrorrrGKDEVD
APC-NH2
QSY 21
Alexa Fluor 647
Caspase
Ac-rkkrrorrrGKDEVD
QSY 21
APC-NH2
647nm
Alexa Fluor 647
665 nm
647nm

Figure 2. Examples of cleavable peptide linker-based probes. (A) Cell penetration of MMP-2 cleavable PDT probe. (B) Schematic diagram of caspase-activatable probe's cleavage.

3. Application of peptide linkers in hydrogels

The development of nature-derived or polymeric materials capable of cellular interaction is important in several applications such as tissue engineering and drug delivery. Hydrogels have received much attention for these applications because of their excellent biocompatibility and convenience in modifications.[20,21] Modifications could be made by diverse methods, where examples using peptides usually involve enzyme sensitive substrates.[22,23]

One example is the fabrication of a MMP sensitive hyaluronic-based hydrogel (Fig. 3), where MMP degradable peptides were used as the crosslinker to mimic the remodeling characteristics of the extracellular matrix (ECM).[24] In addition, cell adhesion peptide RGD was applied for effective cell spreading. In most cases of extremely hydrophilic hydrogels, cells do not preferably attach to the surface because of the

antifouling effect. This MMP sensitive hydrogel was designed to overcome the limits of hyaluronic acid by including the RGD peptide, while the ECM mimicking property was sustained.

Another example involves thrombin-sensitive peptide linker interconnecting polyvinyl alcohol hydrogel.[25] The thrombin-responsive peptide linker was incorporated for the biological signal-responsive drug release system. The hydrogel was designed to react to the elevated thrombin-like activity in infected wound exudates, which would trigger the peptide linker cleavage. Then the disrupted hydrogel system would release gentamicin, an antimicrobial drug.

A

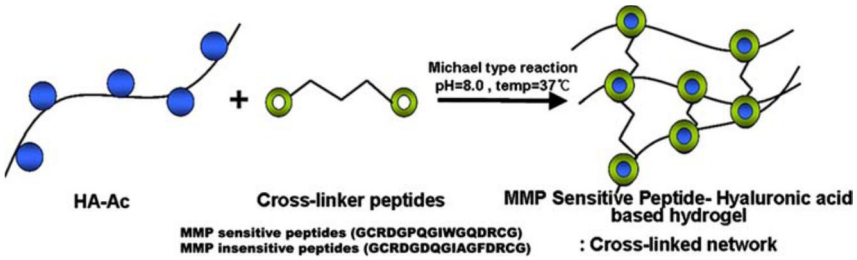

B

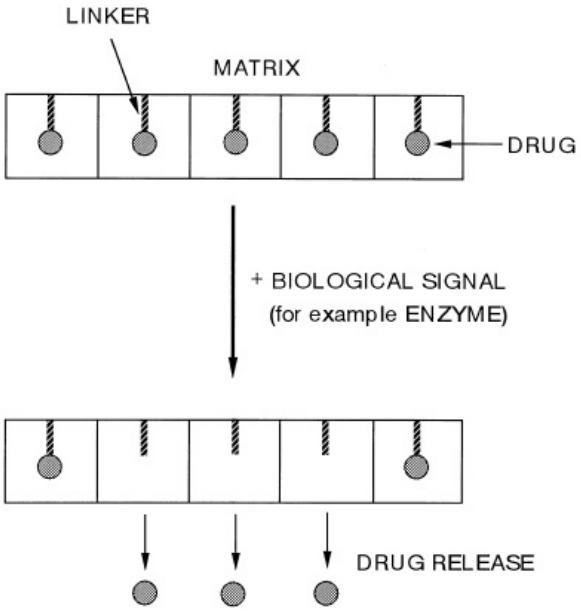

Figure 3. Examples of peptide cross-linked hydrogels. (A) MMP

sensitive peptide/hyaluronic acid based hydrogel. (B) Thrombin-responsive drug releasing hydrogel system.

4. Research Objective

In this thesis, peptide linkers are utilized as powerful tools in the area of biomedical research. First, an enzymatically cleavable cyclic peptide is used to put together a photosensitizer and a quencher for enhanced PDT. Second, tyrosine-rich peptides (TRPs) were tested for the usage as hydrogel linkers.

In chapter 1, enhanced cancer treatment by PDT is described by utilizing the enzymatically cleavable iRGD peptide as a linker. A photosensitizer pyropheophorbide-*a* (Ppa) and a quencher Black-01 (BK01) were conjugated on each end of the iRGD peptide for controlled photosensitization. The goal was to observe the possibility of controlled Ppa activity under specific biological circumstances, which could be led by the molecular design of the cyclic peptide.

In chapter 2, TRPs were used as crosslinking bridges for the

riboflavin induced hyaluronic acid-based hydrogel. In this research, tyramine-conjugated hyaluronic acid (HA-Ty) was used as the backbone hydrogel, where the tyramine residue was chosen because of its crosslinking feasibility with TRPs. Since TRPs have their particular features in self-assembly, they were expected to provide exceptional modifications to the hydrogel when crosslinked together. With the addition of TRPs to HA-Ty hydrogel, a mechanically enhanced scaffold might be fabricated for improved biomedical applications.

Chapter I.
Protease Activatable Peptide Depot for Photodynamic Therapy

1. Introduction

1.1. Basic Principles of Photodynamic Therapy

Photodynamic therapy (PDT) is a less-invasive therapeutic modality relevant for a variety of cancers and pre-cancerous diseases.[26-30] The basic principles behind PDT include excitation of a locally or systemically accumulated photosensitizer (PS) by light to produce a triplet-state PS that can generate cytotoxic singlet oxygen ($^1O_2$) from surrounding oxygen molecules ($^3O_2$) (Fig. 4).[31,32] Since Photofrin® was clinically approved, a number of next-generation photosensitizers have been developed to advance the PDT performance as well as to mitigate its side effects. Among issues raised for PDT, nonspecific phototoxicity arising from untargeted PS residues in the body is recognized as a critical side effect because it causes indiscriminate oxidative damages to normal tissues. As a promising solution to this problem, activatable PSs have been proposed that contain activatable structural units designed to trigger spatiotemporal phototoxic effects in response to tumor microenvironments such

as acidic, hypoxic or reducing conditions, or overexpressed cancer-associated enzymes (Fig. 5).[33-35] In this strategy, nonspecific phototoxicity can be blocked by keeping tumor-untargeted PSs inactive, to allow for highly tumor-selective therapeutic outcomes with minimal side effects on surrounding tissues.

A

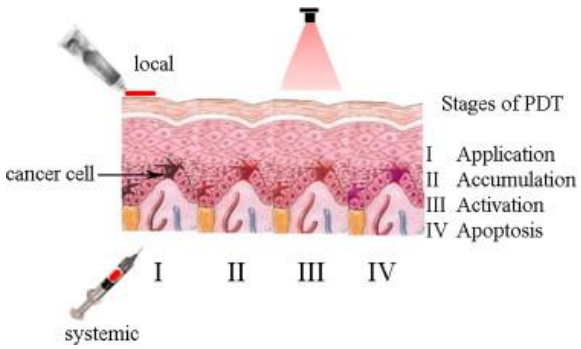

B

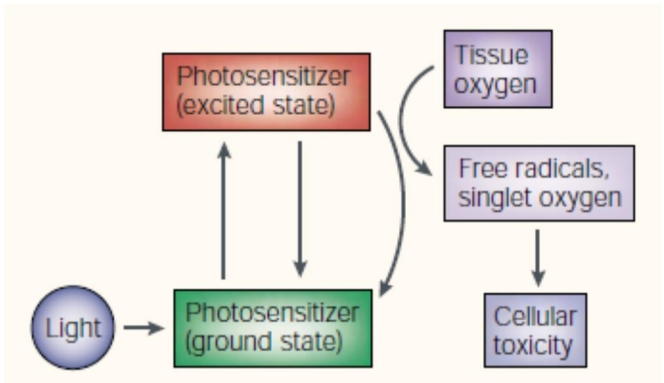

Figure 4. Basic principles of photodynamic therapy. (A) PDT stages including application, accumulation, activation, and apoptosis. (B) Excited state of PS induced by light converts molecular oxygen into singlet oxygen, causing cytotoxic effects.

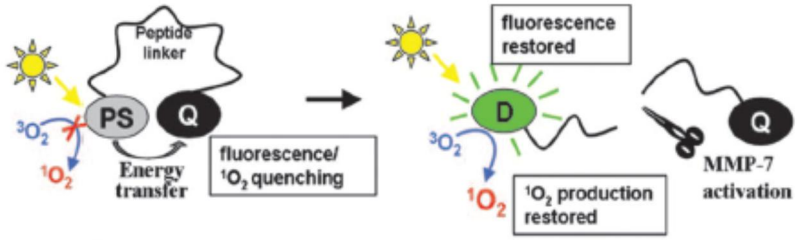

Figure 5. Example of cancer-associated enzyme activatable PS system. PS and quencher is linked by peptide susceptible to MMP-7, which is overexpressed near cancer cells.

1.2. Issues to Overcome for Effective Photodynamic Therapy

Another overlooked issue to be considered for improving PDT is a potential side effect caused by total overdose of repeatedly injected PSs. As opposed to the limited radiation dose in radiotherapy, the PDT procedure is considered harmless and repeatable without critical side effects. In general practice, a session composed of PS injection and laser irradiation is iterated at intervals to ensure optimal therapeutic outcomes, being referred to as an advantage from a clinical view point.[36] Generally, PS injection is demanded in each session of repeated PDT, because the effective PS concentrations at tumor are not retained long enough owing to its clearance as well as photobleaching under light irradiation.[37,38] Although PSs are considered nontoxic, repeated multiple injections could lead to pain, stress, and inconvenience to patients, as well as unexpected side effects by total overdose. Therefore, these concerns are also a critical issue to be solved to take full advantages of PDT as a

less-invasive therapeutic modality. One possible solution would be to fabricate single-injection formulations of PSs that meet the followings; 1) only a single injection autonomously recharges tumor-cleared or photobleached PSs during repeated PDT via sustained release and tumor-targeted delivery, and 2) prior to release, PSs are protected by the formulation from body clearance and photobleaching, to be supplied for sustained tumor recharging. To satisfy these, a number of sustained PS release carriers using nanoparticles or hydrogels have been developed so far (Fig. 6).[31,39,40] In spite of these efforts, however, many issues are yet to be solved (e.g., photobleaching or nonspecific therapeutic activation of carrier-unreleased PSs under light irradiation); thus, repetition of PS injection is still regarded as a standard procedure for repeated PDT.

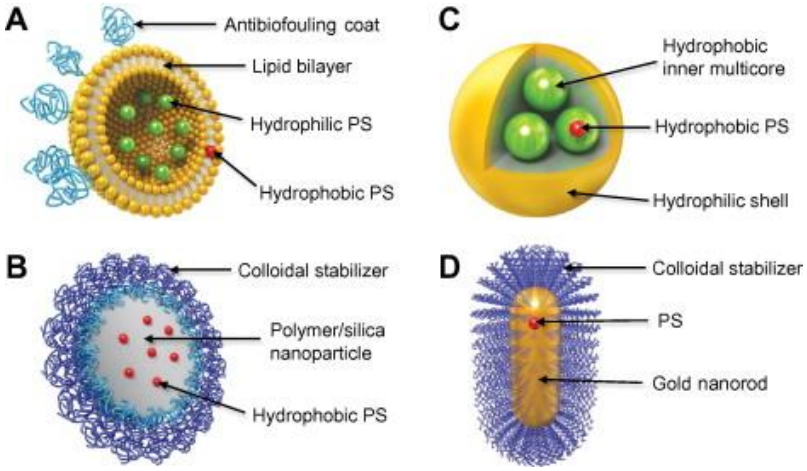

Figure 6. Examples of nanoscale photosensitizer formulations. (A) liposome, (B) polymer/silica nanoparticle, (C) self-assembled nanogel, and (D) gold nanorod.

1.3. Cyclic iRGD Peptide for Photosensitizer Formulation as an Injectable Depot-Forming Monolith

Taking the above issues of PDT into consideration, a simple but very effective PS formulation based on an injectable depot-forming multifunctional peptide was devised. In a recent study, cyclic internalizing RGD peptide (iRGD)-based probe that has multiple functions such as cancer cell-specific targeting, internalization, and fluorescence activation was developed (Fig. 7).[41,42] Such iRGD-driven multiple functions were shown to work cooperatively to improve the precision of diagnostic cancer imaging. Adopting the versatile molecular platform, a similar type of iRGD monolith (Ppa-iRGDC-BK01) that is equipped with a PS (pyropheophorbide-a; Ppa) and a quencher (BK01) on a cyclic iRGD backbone (Scheme 1) was designed, where BK01 is chosen to quench the photosensitivity of Ppa through intramolecular fluorescence resonance energy transfer (FRET). As an activatable PS, Ppa-iRGDC-BK01 is designed so that its molecular activities (cancer cell internalization and

photosensitization) are initially inactive but able to be activated by tumor targeting and subsequent tumoral proteolytic/reductive cleavages of the iRGD cycle (Fig. 8A). Another new and unique feature of Ppa-iRGDC-BK01 is a thermally triggered phase transition that enables it to be implanted as an in-situ self-aggregated depot when its own solution is exposed to body temperature upon injection. The consequent iRGD-driven monolithic combination between tumor-selective therapeutic activation and in situ depot formation attains long-term sustained and autonomous tumor re-photosensitization for repeated PDT.

A

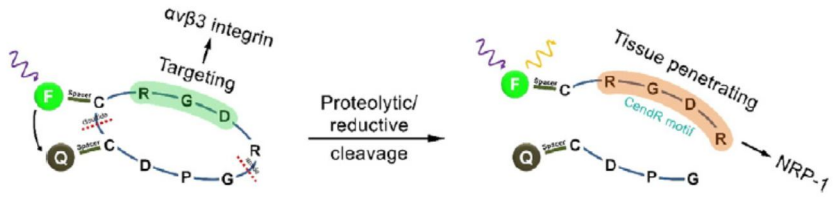

B

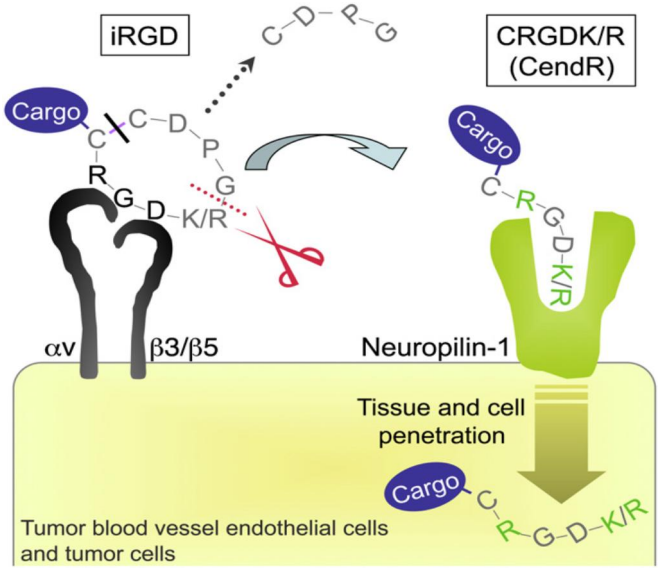

Figure 7. Cyclic iRGD based peptide probe. (A) Dye/quencher combination linked by iRGD peptide, with multiple functions for effective cancer diagnostics. (B) Schematic diagram of the internalization mechanism of cyclic iRGD peptide.

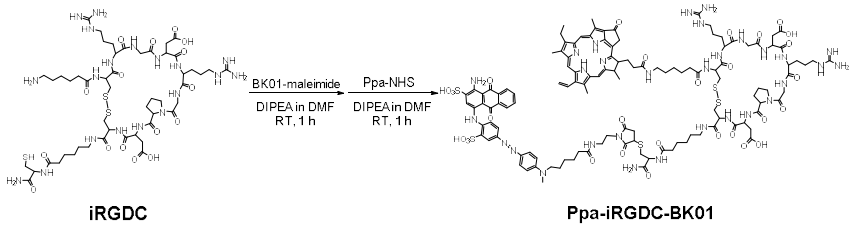

Scheme 1. Synthetic routes and peptide structure for Ppa-iRGDC-BK01.

1.4. Research Objective

The depot strategy offers another benefit that the PS and FRET quencher units of Ppa-iRGDC-BK01 are densely packed within the self-aggregated depot. Such a single-component dense assembly maximizes the proximity among Ppa and BK01 units and thus enhances the photosensitivity quenching by inducing additional intermolecular FRET/self-quenching interactions, in addition to the intrinsic intramolecular FRET quenching. The resulting multiple-quenching process is so efficient to prevail over other photophysical/photochemical pathways, which tightly prevents unnecessary phototoxic effects and photobleaching of the depot-stocked PS before release. In this study, it is demonstrated that the overall beneficial features derived from the design of Ppa-iRGDC-BK01 offer high therapeutic efficacy, precision and safety for repeated PDT through simple treatment practice composed of one-time PS injection and multiple light irradiations (Fig. 8B).

A

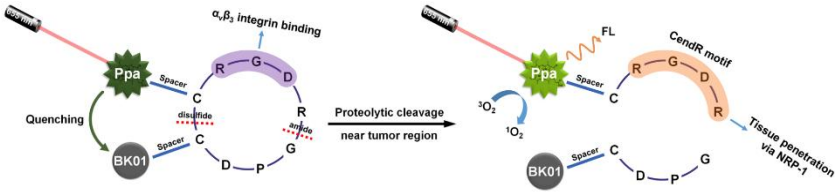

B

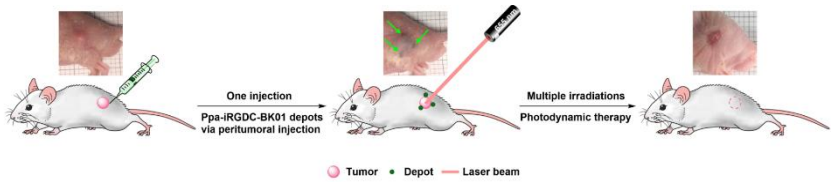

Figure 8. (A) Schematic process of activatable singlet oxygen generation and fluorescence recovery of Ppa-iRGDC-BK01. (B) Schematic diagram of depot formation of Ppa-iRGDC-BK01 after one peritumoral injection and multiple PDT treatment.

2. Experimental Section

2.1. Chemicals and Materials

Unless otherwise noted, all chemical reagents and solvents were purchased from Sigma-Aldrich and TCI and used without further purification. iRGD peptide (iRGDC, H-Ahx-CRGDRGPDC-Ahx-C-NH_2) and control peptide (ConC, H-Ahx-CGGGGGPDC-Ahx-C-NH_2) were customized and purchased from Peptron, Inc. (Korea). Pyropheophorbide-*a* was purchased from Frontier Scientific Inc. (USA), and QFlamma Black-I maleimide as a quencher was purchased from BioActs (Korea). Absorption/emission spectra were recorded on Agilent 8453 UV-visible spectrometer (Agilent, USA) and the F-7000 fluorescence spectrophotometer (Hitachi, Japan). U-87 MG cell line was obtained from Korean Cell Line Bank and cultivated in Roswell Park Memorial Institute (RPMI) 1640 medium supplemented with 10% FBS and 1% antibiotic (penicillin-streptomycin) in a humidified 5% CO_2 incubator at 37 °C. All *in vivo* data were

taken on an IVIS Spectrum imaging system (Caliper, USA).

2.2. Synthesis of Ppa-iRGDC-BK01 and Control Peptides

Ppa-iRGDC-BK01 was synthesized following previous synthetic strategy,[17] BK01-maleimide (7.1 mg, 8.4 μmol) was coupled with the thiol moiety of the *C*-terminal cysteine of iRGDC (10 mg, 7.6 μmol) in DMF (1 mL) with DIPEA (2 μL, 11 μmol). The mixture was stirred at room temperature for 1 h, and reaction completion was monitored by HPLC. After ether precipitation, NHS-activated pyropheophorbide-a (Ppa-NHS, 5.3 mg, 8.4 μmol) prepared as previously described[26] was conjugated on the free amine of the *N*-terminal of iRGDC with DIPEA (2 μL, 11 μmol) in DMF (1 mL). The reaction was performed at room temperature for 1 h and monitored by HPLC analysis until the starting peptide peak disappeared. After ether precipitation, the crude peptide was purified with HPLC. For the peptide analysis, a flow rate of 1.0 mL/min and a 20 min-gradient of 10–80% of solvent B followed by a 5 min-constant

flow of 100% solvent B (solvent A, 0.1% TFA in water; solvent B, 0.1% TFA in acetonitrile) were used with XBridge BEH C18 Column (10 μm, 150 mm × 4.6 mm). For the peptide purification, a flow rate of 4.0 mL/min and a 20 min-gradient of 20–80% of solvent B followed by a 5 min-constant flow of 100% solvent B (solvent A, 0.1% TFA in water; solvent B, 0.1% TFA in acetonitrile) were used with XBridge BEH130 Prep C18 (10 μm, 250 mm × 10 mm). Absorbance was measured at 230 nm, and fluorescence detection used excitation at 670 nm and emission at 690 nm. The lyophilized peptide was obtained from freeze drying of HPLC fraction containing the product (3.5 mg, yield: 20%). The final peptide (Ppa-iRGDC-BK01) was identified by HRMS (calculated exact mass = 1332.5129 for $C_{122}H_{156}N_{30}O_{29}S_5$ ($[M+2H]^{2+}$) and 888.6779 for $C_{122}H_{157}N_{30}O_{29}S_5$ ($[M+3H]^{3+}$), found 1333.0144 and 889.0108). Ppa-iRGDC, peptide without the quencher system, was synthesized by treating iRGDC (3 mg, 2.3 μmol) with Ppa-NHS (1.6 mg, 2.5 μmol) and DIPEA (2 μL, 11 μmol) in DMF (1mL). The mixture was stirred at room temperature for 1 h and

monitored by HPLC analysis. After ether precipitation, the peptide was purified by HPLC. HPLC conditions for analysis and purification of the peptide were the same as used for Ppa-iRGDC-BK01. The final lyophilized Ppa-iRGDC was obtained by freeze drying the HPLC fraction containing the product (2.6 mg, yield: 62%). Ppa-iRGDC was analyzed by MALDI-TOF (calculated exact mass = 1820.8187 for $C_{83}H_{118}N_{23}O_{18}S_3$ (Ppa-iRGDC) $[M+H]^+$, found 1821.3630).

Ppa-ConC-BK01, control peptide without both RGD sequence and CendR motif, was synthesized by the same procedure as for Ppa-iRGDC-BK01, using ConC (2.7 mg, 2.5 μmol). The final lyophilized peptide was obtained in 33% yield (2.1 mg). Ppa-ConC-BK01 was analyzed by MALDI-TOF (calculated exact mass = 2407.8532 for $C_{112}H_{135}N_{24}O_{27}S_5$ (Ppa-ConC-BK01) $[M+H]^+$ and 1922.8545 for [M-azo group+H]$^+$, found 2407.5589 and 1922.4062).

2.3. Time Correlated Single Photon Counting (TCSPC)

TCSPC was conducted for the measurement of time-resolved fluorescence of Ppa, Ppa-iRGDC-BK01, Ppa-iRGDC peptide dissolved in DMSO or PBS (5% DMSO) with FL920 from Edinburgh Instruments. The PL decay times of Ppa were obtained at 678 nm emission with the excitation source of 375 nm by the use of picosecond pulsed diode laser (EPL-470) and calculated by the F900 program with an instrument response function (IRF).

2.4. Singlet oxygen generation

Singlet oxygen generation (SOG) was estimated by observing a decrease in the absorbance of the mixed *p*-nitrosodimethylaniline (RNO) at 440 nm under 655 nm laser excitation (200 mW/cm^2, Changchun New Industries Optoelectronics Tech. Co., Ltd., China). After incubation of the Ppa-iRGDC-BK01 (0.4 mM, PBS (5% DMSO)) in the absence or presence of excessive trypsin (10 μg/mL) and DTT (10 eq) for 1 h, the aqueous mixtures for SOG estimation were prepared by mixing 0.21 mL of Ppa-iRGDC-BK01 solutions with 0.11 mL of RNO solution (0.12 mM), 0.7 mL of histidine solution (0.03 M), and 0.18 mL of water. Laser excitation at 655 nm was performed by irradiating the collimated laser beam through the sample. For preparation of the delayed treatment sample, the Ppa-iRGDC-BK01 solution was irradiated with a 655 nm laser for 15 min before incubation with excessive trypsin and DTT for 1 h. The mixture for SOG estimation was prepared by the same procedure, and then the RNO absorbance was measured under the same irradiation condition.

2.5. *In vitro* cellular uptake

A human primary glioblastoma (U-87 MG) cell line was maintained in RPMI 1640 medium supplemented with 10% FBS and 1% antibiotic (penicillin-streptomycin) in a humidified 5% CO_2 incubator at 37 ℃. The cells were seeded (5×10^4 cells/well) onto 35 mm coverglass bottom dishes and allowed to grow until 70% confluence. After washing with PBS (pH 7.4) twice, the cells were incubated in 2.0 mL of serum-free medium containing Ppa-iRGDC-BK01 or Ppa-ConC-BK01 (each 10 μM) for 2 h. The treated cells were washed twice with PBS (pH 7.4), fixed with 4% (v/v) paraformaldehyde for 5 min, and stained with DAPI for 3 min at room temperature. The fluorescence images were obtained using a LEICA DMI3000B microscope equipped with a Nuance FX multispectral imaging system (CRI, USA).

2.6. *In vitro* dark and phototoxicity assay

U-87 MG cells were seeded (1×10^4 cells/well) onto 96-well plates, and incubated for 24 h. After replacing the culture medium with 200 μL of serum-free medium containing Ppa-iRGDC-BK01 or Ppa-ConC-BK01 (each 10 μM), the treated cells were incubated for 2 h at 37 ℃. The cells were washed with fresh medium, and irradiated with laser (655 nm, 200 mW/cm^2, each well for 5 min). And then the cells were further incubated for another 3 h to determine the phototoxicity. For dark-toxicity, the cells were prepared following the same procedure without laser irradiation. At last, each well was treated with 20 μL of CCK-8 reagent and incubated for 1 h, and then absorbance was measured at 450 nm using SpectraMax M2 (Molecular Devices, USA).

2.7. Animal experiments

The animal studies have been approved by the animal care and use committee of Korea Institute of Science and Technology, and all handling of mice was performed in accordance with the institutional regulations. For tumor models, BALB/c nude mice (male, 5 weeks of age, Orient Bio Inc. Korea) were anaesthetized with intraperitoneal injection of the solution (300 μL) of tiletamine hydrochloride (1 mg/mL), zolazepam hydrochloride (1 mg/mL), and xylazine hydrochloride (0.2 mg/mL) in saline. Tumor xenografts were created by subcutaneous injection of U-87 MG cells (1×10^7 cells in 80 μL of culture medium) into the thigh. After 2 weeks, Ppa-iRGDC-BK01 (10 nmol, 60 μL) was peritumorally injected at 3 points around the tumor. The behaviors of fluorescence activation and accumulation of Ppa-iRGDC-BK01 near tumor were monitored for up to 12 days with anaesthetized mice by IVIS Spectrum equipped with excitation (675/30 nm) and emission (720/20 nm) filters. To evaluate the tissue distribution of internalized peptides, major organs and tumors were dissected from mice at pre-determined time points.

2.7. *In vivo* photodynamic therapy

After xenograft model preparation (2 weeks), peritumoral injection with Ppa-iRGDC-BK01 (10 nmol), Ppa-iRGDC (10 nmol), Ppa-ConC-BK01 (10 nmol), or PBS solution was carried out at 3 points around the tumor (60 μL total injection volume per mouse). Four groups of the U-87 MG tumor xenograft mice were irradiated with laser (655 nm, 200 mW/cm^2) for 10 min at 2 d post-injection. This operation was repeated every two days for all groups, five times in total. Before and after irradiation in each PDT treatment, the changes of the fluorescence were monitored by using IVIS Spectrum. The tumor volume of each mouse was measured with a digital caliper and calculated (width × length × height × 1/2) for 14 d. As control groups without laser irradiation, the mice treated with Ppa-iRGDC-BK01 or PBS were prepared following the same procedure to compare the tumor volume. The tumor and major organs (liver, lung, spleen, kidney, heart, and tumor) were resected at 2 weeks after peritumoral injection and imaged by IVIS Spectrum.

For histological analysis, the major organs were harvested from U-87 MG tumor-bearing mice treated with PBS (control) and the Ppa-iRGDC-BK01 under laser irradiation 14 d after peritumoral injection. The organs were fixed with 4% formaldehyde solution, embedded in paraffin, and sliced into ~5 μm thickness. The sections were stained with haematoxylin and eosin (H&E), and visualized by optical microscope (BX 51, Olympus, Japan).

3. Results and Discussion

3.1. Synthesis of Activatable Ppa-iRGDC-BK01

In order to build a tumor-specific activatable system, cyclic iRGD peptide (c(CRGDRGPDC)) was chosen as an activatable frame that has cancer cell-specific targeting and internalizing abilities triggered by proteolytic/reductive cleavages.[41] Following the synthetic strategy for an activatable probe previously reported,[42] BK01-maleimide was conjugated to the C-terminal cysteine of iRGDC peptide to yield iRGDC-BK01, and then next coupling of the NHS-activated pyropheophorbide-a (Ppa) to the N-terminal free amine of iRGDC peptide resulted in the final Ppa-iRGDC-BK01 (Scheme 1). As control peptides, Ppa-iRGDC without quencher and Ppa-ConC-BK01 synthesized from a control peptide sequence (c(CGGGGGPDC)) without $\alpha_v\beta_3$ integrin targeting (RGD) and NRP-1-mediated internalizing (CendR, R/KXXR/K) functions were prepared in the same procedures as Ppa-iRGDC-BK01 (Scheme 4). All the obtained

peptides were purified by preparative HPLC and identified by MALDI-TOF mass or HRMS (Supporting Information).

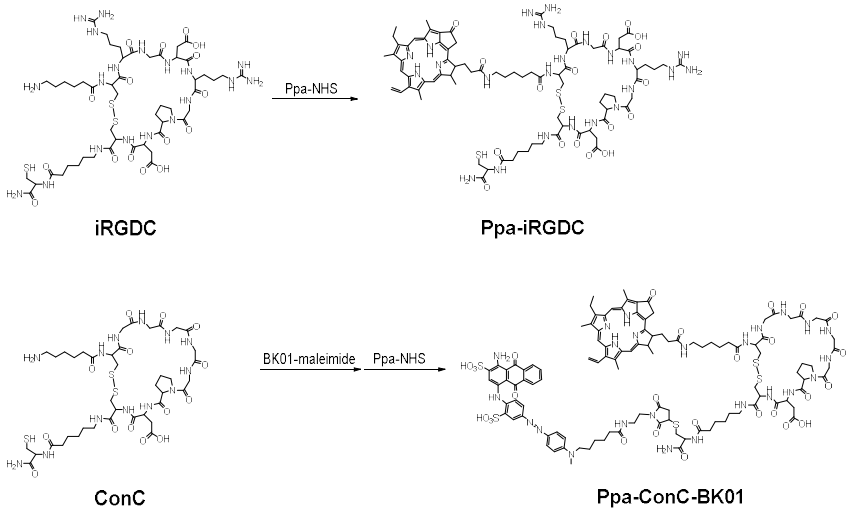

Scheme 2. Synthetic routes and peptide structure for Ppa-iRGDC and Ppa-ConC-BK01.

3.2. Fluorescence Activation of Ppa-iRGDC-BK01 under Laser Irradiation

In Ppa-iRGDC-BK01, the PS unit (Ppa) has dual optical activities arising from the same photoexcited state, i.e., photosensitization of $^1O_2$ and fluorescence emission, both of which were shown to be efficiently quenched by BK01 in pH 7.4 PBS (Fig. 9A). To investigate the recovery of the quenched optical activities through proteolytic/reductive cleavages, Ppa-iRGDC-BK01 was incubated in the presence of excess trypsin and DTT, and measured the temporal evolution of Ppa fluorescence. As shown in Figure 9A, the Ppa fluorescence was gradually intensified with time to show more than an 18-fold intensity increase over that of the initial quenched state 1 h after incubation. This result proves that the fluorescence activation of the Ppa-iRGDC-BK01 is well operative by the cleavage of both disulfide and amide bonds of the iRGD peptide.

Another quencher function intended, is to protect the photosensitizer within a depot under photo-irradiation. To

confirm the quencher effect against photo-irradiation, the Ppa-iRGDC-BK01 or the Ppa-iRGDC dissolved in PBS was exposed under laser irradiation (655 nm, 200 mW/cm^2) for 20 min. Then, the fluorescence of Ppa was measured at each time point after incubation with trypsin and DTT for 1 h. As laser irradiation time increased, the fluorescence of the Ppa-iRGDC without quencher conjugation was gradually bleached and almost degraded in 20 min (Fig. 9B). In contrast, the Ppa-iRGDC-BK01 with quencher stably maintained its fluorescence over ~92 % for 10 min under laser irradiation, validating that the quencher could effectively protect the photosensitizer from direct laser irradiation. For in-depth evaluation of the fluorescence quenching, the fluorescence relaxation kinetics of Ppa-iRGDC-BK01 and Ppa-iRGDC were examined using time-correlated single photon counting (TCSPC). To check the self-quenching effect of Ppa by aggregation, peptide probes were dissolved in DMSO as a homogeneous solution or PBS (1% DMSO) where amphiphilic photosensitizers partially formed aggregated species.[43] As shown Figure 10, the fluorescence life time of the Ppa-iRGDC in PBS decreased from

that in homogeneous solution (DMSO), which is attributable to self-quenching of Ppa fluorescence (average fluorescence life time (τ) = 7.2 ns $\rightarrow$ 6.2 ns). Comparing the fluorescence decay between the Ppa-iRGDC-BK01 and the Ppa-iRGDC in homogeneous solution (DMSO), it was confirmed that the quencher could sharply shorten the fluorescence life time of the Ppa via fast radiationless relaxation of excitation energy. Taken together, the photosensitizer within the Ppa-iRGDC-BK01 is expected to stably exist in a depot without photo-bleaching by the combination of quenching from quencher and self-quenching even under photo-irradiation.

A

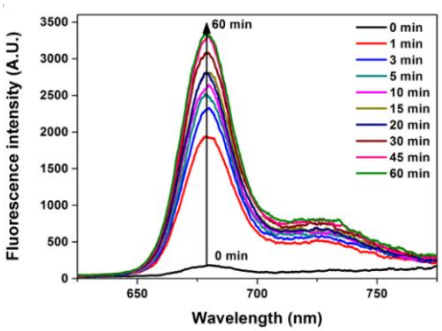

B

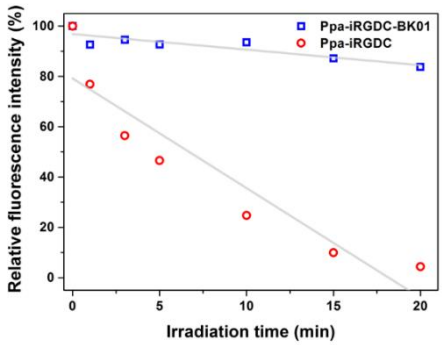

Figure 9. (A) Fluorescence dequenching of Ppa-iRGDC-BK01 (10 μM) under trypsin (1 μg/mL), DTT (10 eq) treatment at 37°C in pH 7.4 PBS (5% DMSO) (ex/em = 405/672 nm). (B) Time dependent fluorescence degradation of Ppa-iRGDC-BK01, and Ppa-iRGDC under laser irradiation (655 nm, 200 mW/cm^2). The fluorescence was measured after trypsin (1 μg/mL) and DTT (10 eq) treatment (ex/em = 405/672 nm).

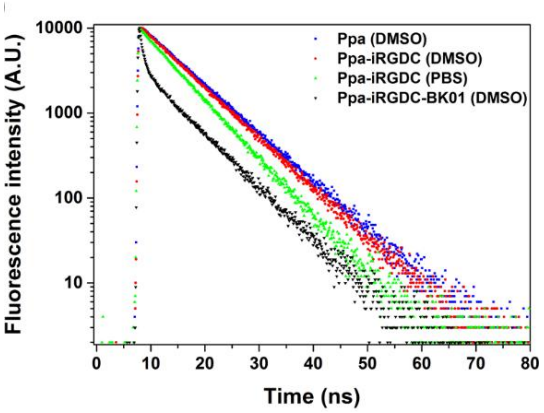

Figure 10. Fluorescence relaxation kinetics of Ppa in DMSO (blue, monoexponential decay, $\tau 1$ = 7.6 ns) , Ppa-iRGDC in DMSO (red, monoexponential decay, $\tau 1$ = 7.2 ns), Ppa-iRGDC in PBS (1% DMSO) (green, monoexponential decay, $\tau 1$ = 6.2 ns), and Ppa-iRGDC-BK01 in DMSO (black, biexponential decay, $\tau 1$ = 0.6 ns , $\tau 2$ = 6.8 ns).

3.3. Singlet Oxygen Generation by Ppa-iRGDC-BK01

Next, the singlet oxygen ($^1O_2$) generation of the Ppa-iRGDC-BK01 was estimated by ρ-nitrosodimethylaniline (RNO) bleaching assay in the presence of histidine.[44] The absorbance change of RNO was monitored at 440 nm under laser irradiation at 655 nm. After incubation with excessive trypsin and DTT, the Ppa-iRGDC-BK01 efficiently produced $^1O_2$ that engendered RNO bleaching via photo-chemical oxidation (Fig. 11A). Without any cleavage, however, the photosensitizer in desensitized state generated negligible $^1O_2$ under laser irradiation for 15 min, demonstrating that the $^1O_2$ generation as well as the fluorescence turn-on of the Ppa-iRGDC-BK01 can be activated by reductive and proteolytic cleavages on the iRGD peptide. To investigate the photosensitization efficiency of the Ppa-iRGDC-BK01 against photo-irradiation in desensitized state, the $^1O_2$ generation was measured using the Ppa-iRGDC-BK01 pre-treated with laser irradiation for 15 min before trypsin and DTT treatment (Fig. 11B). Based on the derived slopes of RNO absorbance plots (–ln

A440) versus irradiation time,[45] the Ppa-iRGDC-BK01 even after laser irradiation still exhibited the good $^1O_2$ generation capability maintaining over 83% efficiency in comparison to the intact one. These results suggest that the Ppa-iRGDC-BK01 hold great potential for PDT use, released from a depot where its $^1O_2$ generation is impervious under photo-irradiation.

A

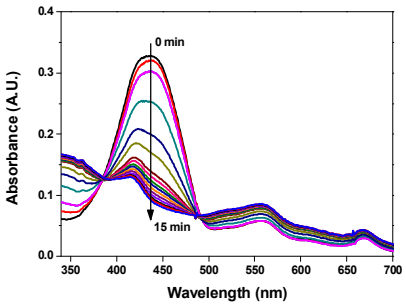
0 min
15 min
Absorbance (A.U.)
Wavelength (nm)
0.0
0.1
0.2
0.3
0.4
350
400
450
500
550
600
650
700

B

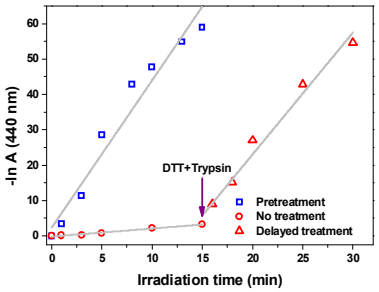
DTT+Trypsin
Pretreatment
No treatment
Delayed treatment
-ln A (440 nm)
Irradiation time (min)
0
10
20
30
40
50
60
0
5
10
15
20
25
30

Figure 11. (A) Photochemical oxidation of RNO by the generated $^1O_2$ from the Ppa-iRGDC-BK01 under laser irradiation (655 nm, 200 mW/cm2) after excessive trypsin and DTT treatment. (B) Temporal dependence of RNO absorbance at 440 nm (-ln A) during irradiation of the Ppa-iRGDC-BK01 pretreated with trypsin&DTT (blue square, slope = 4.16), non-treated (red circle, slope = 0.23), and delayed treated with trypsin&DTT (red triangle, slope = 3.45) under identical laser-irradiation condition. Straight lines are linear fits of the absorbance plots.

3.4. Cellular Uptake and Cell Viability Under Laser Irradiation

Photosensitizer delivery into cancer cells is essential for effective cancer treatment via PDT. To identify the cellular uptake of the photosensitizer, the U-87 MG, a cancer cell line highly expressing both $\alpha_v\beta_3$ integrin and NRP-1,[46] was treated with the Ppa-iRGDC-BK01 for 1 h, and then the fluorescence of the Ppa was observed by fluorescence microscope. As a control, Ppa-ConC-BK01 which has no targeting and internalizing moieties was used. As anticipated, the Ppa fluorescence was clearly shown in the cytoplasm of U-87 MG treated with the Ppa-iRGDC-BK01,

whereas the only traces of the Ppa signal were shown in the Ppa-ConC-BK01-treated one (Fig. 12A). This comparison supports that the delivery of the activated photosensitizer into the cancer cells is well operative via the iRGD-derived multiple functions (cancer targeting, internalization and proteolytic reaction).[41]

Based on good cellular uptake behavior of the Ppa along with the fluorescence recovery via the iRGD peptide, dark- and photo-toxicity of the Ppa-iRGDC-BK01 were assessed by CCK8 assay. After treating U-87 MG cells with Ppa-iRGDC-BK01 or Ppa-ConC-BK01 for 1 h, cell viability was measured in the absence or presence of laser irradiation (Fig. 12B). Regardless peptide sequence, the photosensitizer and quencher-conjugated peptides were non-toxic in the dark. Under laser irradiation, however, the Ppa-iRGDC-BK01 gave higher photo-toxic effect on the U-87 MG cells than control ones, thereby providing potential for *in vivo* PDT.

A

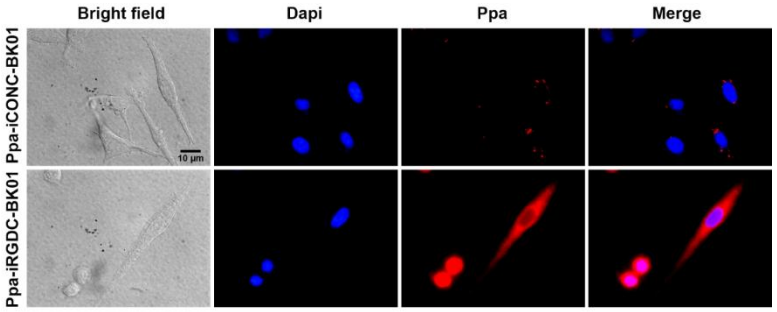
Bright field
Dapi
Ppa
Merge
Ppa-iCONC-BK01
Ppa-iRGDC-BK01
10 μm

B

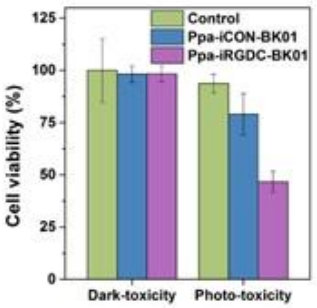

Figure 12. (A) Optical/fluorescence merged images of U-87 MG cells treated with Ppa-ConC-BK01 (top) and Ppa-iRGDC-BK01 (bottom) for 2 h. Red, Ppa; blue, nucleus-staining DAPI. Scale bar: 10 μm. (B) *In vitro* dark- and photo-toxicity of PBS (control), Ppa-iRGDC-BK01 or Ppa-ConC-BK01 against U-87 MG cells. The error bars indicate the standard deviations based on five samples per group.

3.5. Depot Formation and Sustained Release

Given the successful photosensitizer delivery into the cancer cells with effective photo-toxicity, the peptide-based activatable photosensitizer was applied for *in vivo* photodynamic therapy via peritumoral administration. Prior to laser treatment, *in vivo* tumor uptake and behavior of the Ppa-iRGDC-BK01 near tumor environment were investigated. The Ppa-iRGDC-BK01 was

soluble in PBS solution (5% DMSO), but underwent phase transition as the temperature increased. This temperature-triggered aggregation (or coacervation), allowed for the depot formation of the Ppa-iRGDC-BK01 *in vivo*.[47,48] Peritumorally injected into U-87 MG tumor-bearing mice, the Ppa-iRGDC-BK01 was deposited as depots near the tumor tissue (green arrow in Fig. 13C). To examine *in vivo* tumor accumulation of the Ppa-iRGDC-BK01, fluorescence signal of the photosensitizer was tracked for 12 d. The signal which is mostly localized on the tumor region was gradually intensified, reached a peak on the 6th day, and then diminished with time (Fig. 13A, B). Based on *in vitro* results and a previous report,[42] it was assumed that Ppa-iRGDC-BK01 was activated by proteolytic cleavage near tumor environment after targeting on $\alpha_v\beta_3$ integrin, exposing the CendR motif along with the activated photosensitizer that could be internalized into tumor tissue via NRP-1.[41] These results suggested that the Ppa-iRGDC-BK01 depot provided prolonged release of the activated photosensitizer into tumor via iRGD multi-functions,

facilitating multiple irradiations for efficient PDT. To support this argument, the major organs including the tumor were resected at 3 d after peritumoral injection of the Ppa-iRGDC-BK01, and analyzed by IVIS with Ppa fluorescence channel before and after scraping out the depots. As shown Figure 13C, the dequenched fluorescence of the Ppa released from the depots was observed throughout the tumor tissue. Furthermore, the average fluorescence intensity of the Ppa in the tumor did not significantly change even after removing the depots, indicating that the quenched Ppa stably existed inside the depots and the fluorescence signal came from the dequenched Ppa in the tumor, not from the depots.

A

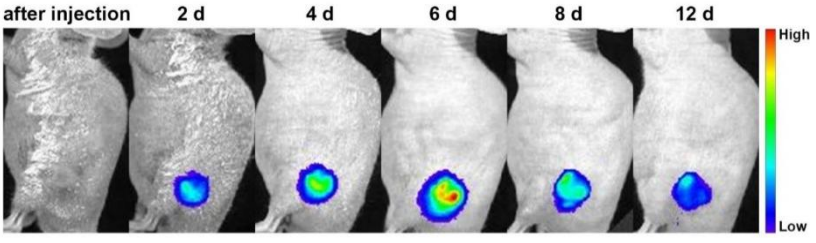

B

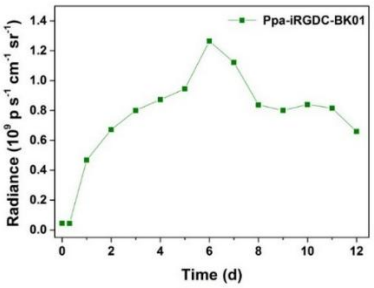

C

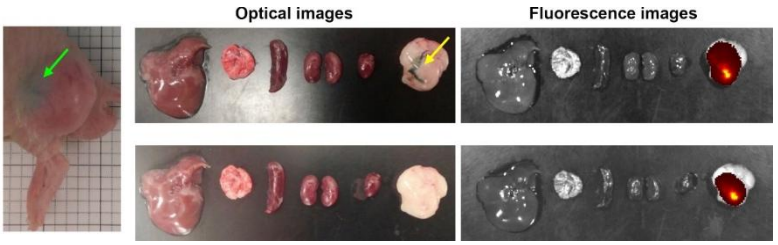

Figure 13. (A) *In vivo* fluorescence images of a U-87 MG tumor-bearing mouse after peritumoral injection of Ppa-iRGDC-BK01, and (B) temporal change of the Ppa fluorescence intensity quantified from ROI at tumor region. (C) Optical image of the depot (green/yellow arrow) and fluorescence signal of internalized Ppa from the depot.

3.5. Single Injection and Multiple Irradiations for PDT

In order to evaluate the *in vivo* PDT efficacy via single injection and multiple irradiations strategy, the Ppa-iRGDC-BK01 was peritumorally injected into U-87 MG tumor bearing

mice (initial tumor size: ~60 mm^3). Based on temporal change of the Ppa fluorescence intensity at tumor region (Fig. 14A), laser irradiation (655 nm, 200 mW/cm^2) was begun 2 days after injection for 10 min, and repeated every other day in quintuplicate. During PDT treatment, the fluorescence intensity change of the activated photosensitizer was monitored, and the degree of tumor growth was measured for 14 d. As controls, PBS (control), Ppa-ConC-BK01, or Ppa-iRGDC was treated into U-87 MG tumor-bearing mice under the same irradiation condition. In general, the photosensitizer was vulnerable to bleaching by photo-sensitization in producing $^1O_2$ under laser irradiation.[49] Due to the depot that allow sustained release of Ppa-iRGDC-BK01, the diminished fluorescence of the Ppa in the tumor after laser irradiation was restored for further PDT treatment until the next irradiation (Fig. 14A,B). In contrast, the Ppa-iRGDC depots without quencher system would be considerably damaged in initial laser irradiation, resulting in low restoration against laser irradiations. Moreover, the Ppa-ConC-BK01 which has no targeting and internalizing moieties

seemed to follow wash-out process. These comparative results validated that the Ppa-iRGDC-BK01 was efficiently protected by the quencher under multiple laser irradiations in the depots *in vivo*.

Such differences of *in vivo* distribution of the activated photosensitizer in tumor under multiple laser irradiations led to different tumor growth patterns during PDT treatment. As shown in Figure 15A, the mice treated with the Ppa-iRGDC or the Ppa-ConC-BK01 exhibited steady tumor growth with slight inflammation trace or no significant therapeutic effect, as similarly observed in the control group under laser irradiation. In stark contrast, tumor growth was completely suppressed with the obvious tumor necrosis sign (scrap on the tumor) in the Ppa-iRGDC-BK01-treated mouse group (Fig. 15A). Furthermore, not even a trace of the tumor was observed near xenografted-site after 30 days (Fig. 15B), demonstrating that the Ppa released from Ppa-iRGDC-BK01 depots were indeed operative to efficiently eradicate the tumor via single injection and multiple irradiations strategy.

After PDT treatment, the mouse organs treated with the Ppa-iRGDC-BK01 under laser irradiation were harvested to evaluate *in vivo* toxicity. No fluorescence signal of the Ppa was observed in major organs except for tumor tissue, and H&E stained major organ slices showed no significant traces of necrosis. Moreover, the tumor treated with Ppa-iRGDC-BK01 without laser irradiation showed almost similar growth pattern to control, indicating that Ppa-iRGDC-BK01 had no *in vivo* dark toxicity. Regardless of laser irradiation and treatment, all mice groups exhibited similar bodyweight change pattern during PDT treatment period of 14 d. All results suggested that the Ppa-iRGDC-BK01 was not accumulative in other organs, being potentially suitable as a PDT drug for *in vivo* uses.

A

B

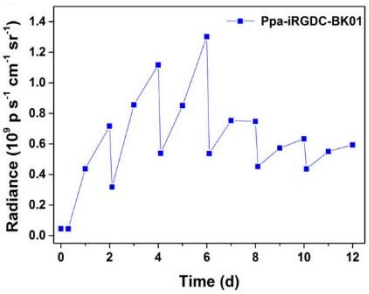

Figure 14. (A) *In vivo* fluorescence images of a U-87 MG tumor-bearing mouse during PDT with Ppa-iRGDC-BK01. Laser irradiation (655 nm, 200 mW/cm^2) for 10 min was performed 5 times every 2 d after peritumoral injection. (B) Temporal change of the Ppa fluorescence intensity quantified by ROI at tumor region treated with Ppa-iRGDC-BK01.

A

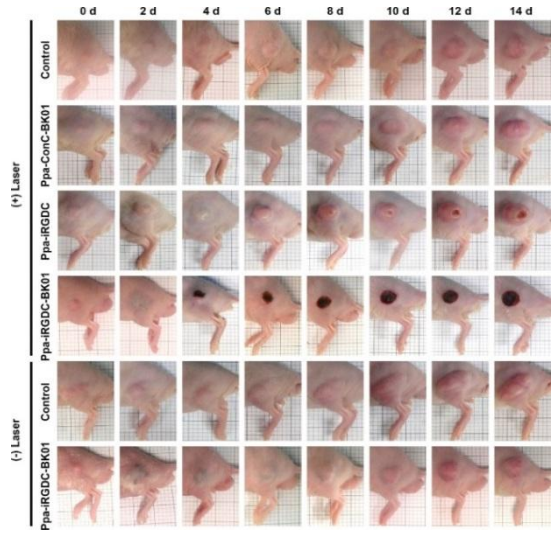

B

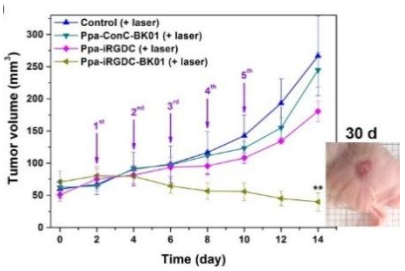

Figure 15. (A) All optical images of U-87 MG tumor-bearing mice treated with PBS (control), Ppa-iRGDC-BK01, Ppa-ConC-BK01, or Ppa-iRGDC for 14 d. PDT operation under 655 nm laser irradiation for 10 min was performed 5 times every 2 d after peritumoral injection. (B) Change of tumor volume examined for 14 d. Arrows indicate the time point of PDT operation.

4. Conclusion

An activatable Ppa-iRGDC-BK01 depot was developed to facilitate sustained release of the activatable photosensitizer into the tumor for highly efficient PDT via single injection and multiple irradiations. The Ppa-iRGDC-BK01 modulated by tumoral proteolytic cleavage showed better delivery of the activated photosensitizer into the cancer cell than that of control with no targeting and internalizing ability, leading to efficacious phototoxicity in cancer cells. Using the aggregation feature of Ppa-iRGDC-BK01, the depot was successfully formed near tumor, where photobleaching of the Ppa-iRGDC-BK01 was prevented by the combination of the quencher and aggregation under laser irradiation. Due to sustained provision of the photosensitizer into the tumor, complete tumor treatment via single injection and multiple irradiations was achieved without any side effect to normal tissue. This combination of the depot and the activatable photosensitizer presents new insight into the PDT strategy to enhance efficacy as well as to relieve pain, broadening PDT applications in further clinical studies.

Chapter II.
Riboflavin-Induced Hyaluronic acid/Peptide Hydrogel for Bio-Applications

1. Introduction

1.1. Hyaluronic Acid Hydrogel for Bio-Applications

Wound dressings made of biodegradable hydrogels have been extensively studied, since moisture environment proved to be essential for successful wound healing.[50] Specially, bio-polymer based hydrogels have been recognized as one of the most ideal dressing materials because of their biocompatibility and hydrating abilities.[51] Among many bio-polymers, hyaluronic acid (HA) exists in the body varying from 1 to 10,000 kDa in molecular weight (Fig. 16) and it is directly related to wound healing as has been reported in numerous studies.[52-56] It is known that HA-enriched fetal wound creates a permissive environment for dermal repair, where multiple factors such as cell migration, cell differentiation, and angiogenesis support the healing process.[57-59] Furthermore, biocompatibility, lack of immunogenicity, and outstanding gel-forming features make HA a promising hydrogel material for bio-medical application.

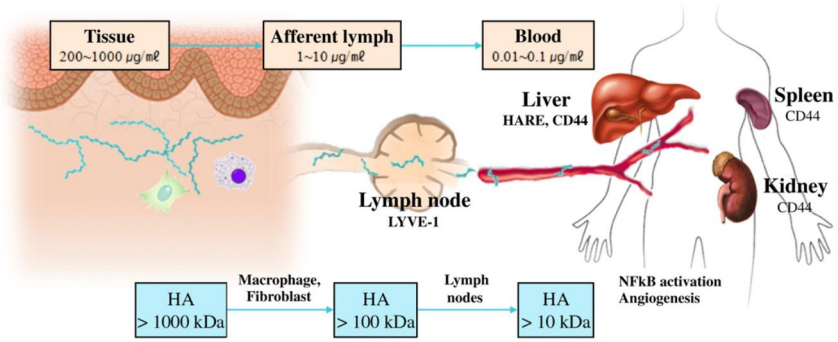

Figure 16. Hyaluronic acid existing in diverse molecular weight throughout the body.

1.2. Riboflavin/UVA based Hydrogel Fabrication

Riboflavin, known as vitamin B_2 (Fig. 17A), is a naturally existing photo-initiator which has been applied in preparation of various photo-crosslinked hydrogels.[60-62] Among them, collagen was subjected to many riboflavin-induced photo-crosslinking studies, where dityrosine formation was involved in the crosslinking mechanism.[47,48] The crosslinking mechanism involves the excitation of riboflavin by light absorption at specific wavelengths (Fig. 17B), which produces tyrosil radicals followed by radical recombination of phenol moeities (Fig. 17C).[63,64] There are numerous other cases of tyramine-conjugated HA (HA-Ty) hydrogels induced by various crosslinking methods.[65-67] So far, studies on riboflavin-based HA-Ty hydrogels have not been reported. This is probably because the reactive oxygen species (ROS) produced by irradiated riboflavin is responsible for the degradation of HA.[68,69] Nevertheless, the combination of riboflavin and HA seems to be interesting for the wound healing application.

A

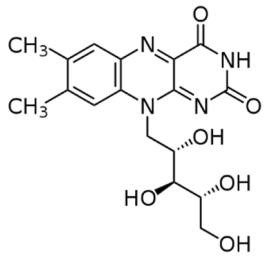

B

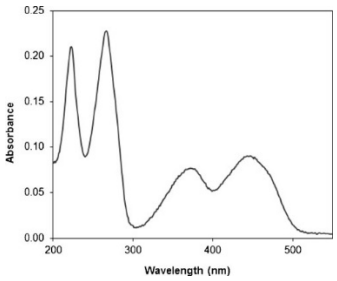

C

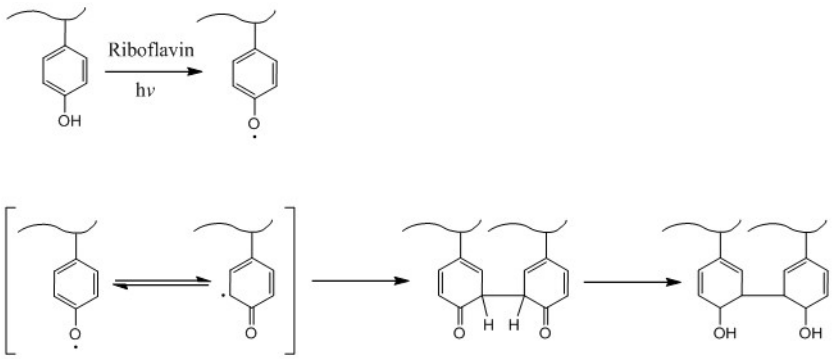

Figure 17. (A) Structure and (B) UV/Vis absorption spectra of riboflavin. (C) Mechanism of riboflavin and UV induced di-tyrosine crosslinking.

1.3. Tyrosine-Rich Peptides as Modulators for HA-Ty Hydrogel

Dityrosines are naturally found in resilin, which show outstanding properties in elasticity and energy storage.[70] This is why numerous studies in crosslinked hydrogels using dityrosine linkage exist. While most of the researches on hydrogels involve mixing of different kinds of polymers, there is no case in the study of using peptide as a crosslinking additive. Tyrosine-rich peptides (TRPs) are peptides of various lengths having repeating tyrosine units.[71] The previous works on TRPs have focused on the two-dimensional self-assembled structure. Since TRPs could be crosslinked with HA-Ty, it was assumed that the self-assembling features of TRPs could cause diverse effects in the hydrogel environment. Therefore, modulations in the mechanical properties of the hydrogel were expected by addition of TRPs.

1.4. GHK-Cu for effective Wound Healing

For the functional advancement of the hydrogel, a well-studied wound healing agent GHK-Cu peptide was utilized.[72,73] GHK-Cu is a naturally existing tripeptide which has specific wound healing property by increasing proliferative factors in human keratinocytes.[74] HA is known to possess wound healing abilities, but this is a HA receptor mediated system which requires low molecular weight HA.[75-77] So, when using high molecular weight HA based scaffolds, wound healing is a timely process. In a previous research, decreased HA levels at acute wounds were observed at an early postwound stage (Fig. 18), suggesting that providing exogenous HA at this time point is necessary for effective wound healing.[78] Under these circumstances, an additional wound healing agent that could boost the healing process seems necessary. As an additive, GHK-Cu would give a synergistic effect with HA in wound healing.

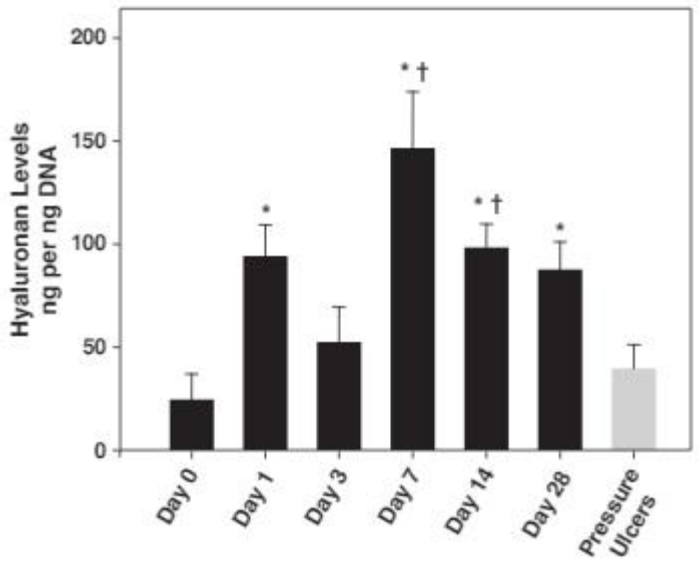

Figure 18. Quantified HA levels in acute wound (black bars) and chronic wound (grey bar).

1.4. Research Objective

HA-Ty modulated with TRPs in hydrogel formation is expected to provide enhanced rheometric characteristics. The modified HA-Ty/TRP hydrogel could show improved wound healing efficacy with or without the addition of the wound healing agent, GHK-Cu. Riboflavin-sensitized photo-crosslinking was utilized as a gelation strategy, where riboflavin induces covalent linkages between the phenolic groups of conjugated tyramines under UV irradiation. TRPs, as an additive, enhanced the mechanical properties of the HA-Ty hydrogel because the tyrosine residues could also participate in the crosslinking with the phenol moieties of the HA-Ty. In this study, HA-Ty/TRP hybrid hydrogels were tested on human cell lines and mouse wound model as a plausible healing agent for wound injuries.

2. Experimental Section

2.1. Materials and Instrumentation

Unless otherwise noted, all solvents and reagents were obtained from commercial suppliers and used without further purification. Hyaluronic acid (HA, sodium salt, Mw 1200 kDa) was provided from SK Bioland (Cheon-an, Korea) and purchased from Lifecore Biomedical, LLC (Minnesota, USA). N-(3-Dimethylaminopropyl)-N′-ethylcarbodiimide hydrochloride 98% (EDC), riboflavin 5'-phosphate sodium, 3-(4,5-dimethylthiazol-2-yl)-2,5-diphenyltetrazoluim bromide, hyaluronidase and thermolysin were purchased from Sigma Aldrich, Co. (St. Louis, USA). N-hydroxysulfosuccinimide Sodium Salt was purchased from Tokyo Chemical Industry Co. (Tokyo, Japan), and tyramine hydrochloride, 99% was purchased from Acros Organics (Geel, Belgium). Dulbecco's Modified Eagle's Medium (DMEM) and Phosphate Buffer Saline (PBS) were purchased from Welgene, Inc. (Gyeongsan,

Korea), and fetal bovine serum (FBS) was purchased from Thermo Scientific HyClone (UT, USA). Transwell® was purchased from Corning Inc. (New York, USA). Finally, customized peptides were purchased from BeadTech Inc. (Ansan, Korea). UV irradiation was performed by LightningCure 2000 (Hamamatsu, Japan), and rheometric analysis was performed by Discovery Hybrid Rheometer-3 (TA Instruments, USA).

2.2. Synthesis and Characterization of Tyramine-conjugated Hyaluronic Acid

HA-Ty conjugates were prepared by coupling HA with tyramine hydrochloride via EDC/NHS coupling reaction. HA sodium salt (1.0 g, 2.5 mmol carboxylic acid groups) was dissolved in 100 mL of distilled water (0.01 mol L−1). To the solution, EDC (1437.75 mg, 7.5 mmol) and NHS (863.175 mg, 7.5 mmol), and tyramine hydrochloride (1302.3 mg, 7.5 mmol) were added. The resulting solution was stirred overnight at room temperature. The reaction mixture was purified by step by step ultrafiltration (MWCO 12000) with 5 L of 100 mmol•L−1 salt solution, 5 L of 18 mol•L−1 EtOH solution, and 5 L of distilled water. The resulting HA-Ty conjugate was collected as solid powder after freeze-drying. The degree of substitution of Ty residues in HA-Ty conjugate, defined as the number of tyramine moieties per 100 repeating units of HA, was calculated to be 11, as determined by 1H NMR. 1H NMR (D2O): δ 1.99 (acetyl methyl protons), 6.8 and 7.2 (aromatic protons of tyramine moieties). Conjugation of tyramine to the carboxylic

acid of HA was once again confirmed by UV spectroscopy. Tyramine hydrochloride was dissolved in PBS buffer at pH 7.4 and diluted to 0.1 μM ~ 10 μM, and UV absorption survey scan was performed to reveal a distinctive 274 nm absorbance. None substituted HA was dissolved in PBS buffer at pH 7.4 (1 wt%), and diluted to 0.1 ~ 1 wt%. UV absorption survey scan was performed to reveal no significant absorbance around 274 nm.

2.3. Fabrication of HA-Ty Hydrogel by Riboflavin and UVA

Hydrogels were prepared by photo-oxidation crosslinking of the phenol moieties induced by riboflavin and UVA irradiation. 990 μL of 1 % (w/v) HA-Ty and 10 μL of riboflavin 5'-phosphate (0.1 mg/mL) was mixed and irradiated with 365 nm UVA for 2 hr. The gelation process monitored by UV absorbance transition was verified by crosslinking just the tyramine hydrochloride solution with riboflavin. Tyramine hydrochloride was dissolved in PBS (pH 7.4) with riboflavin in a UV cuvette and crosslinked under 365 nm irradiation. Survey scan was performed at dedicated time points. The red arrow indicates the newly appearing absorbance band during the crosslinking of tyramine molecule. When fabricating HA-Ty/peptide mixed hydrogels, TRPs (DYC7, YC7, YH7, YA5, YC5) were mixed into the HA-Ty solution in 0.1 mM concentration before crosslinking.

2.4. *In vitro* Swelling & Degradation Tests

HA-Ty hydrogels with different TRPs (DYC7, YC7, YH7, YA5, and YC5) added in 0.1 mM concentration were prepared. Swelling experiments were performed by measuring the weight increase of dried hydrogels. Lyophilized hydrogels were placed in 1 mL distilled water at 25 ˚C. The swelling ratio (S%) of hydrogels in distilled water was calculated using $S\% = [(W_t - W_0]/W_0)]100$, where W_t is the weight of the swollen hydrogel at time t, and W_0 is the weight of the dry gel at time 0. Hydrogel made of only HA-Ty was used as control. Degradation tests were performed by measuring the weight decrease of pre-fabricated hydrogels. Hydrogels were placed in 1 mL PBS (pH 7.4) containing 0.1 U hyaluronidase at 37˚C. The percentage of the remaining hydrogels was calculated in contrast to the starting weight.

2.5. Rheological Analysis

Oscillatory shear measurements of the storage modulus (G') was obtained at room temperature using a constant stress rheometer (Discovery Hybrid Rheometer-3 from TA Instruments, USA). For measurements, the hydrogel samples with the defined shape of 20 mm diameter and 5 mm thickness were prepared. Cured hydrogel was placed on the lower rheometer stage, and the upper rheometer fixture (diameter 20 mm) was lowered until it made contact with the top surface of the sample. Then G' was measured at oscillation frequency 1 Hz in a stress sweep test from 0.1 to 100 Pa. The stress sweep was performed in order to determine the limit of the linear viscoelastic regime. All G' measurements were obtained in triplicates and error bars in all figures represent the sample standard deviation for the values averaged.

2.5. Cytotoxicity and Cell Proliferation Assay

Normal human fibroblasts were isolated from human foreskins obtained during circumcision, which was carried out under informed consent. Skin specimens were processed according to the method described,[79] and modified in Seoul National University Bundang Hospital laboratory using thermolysin. To investigate the biocompatibility of the hydrogel components, fibroblasts were used to perform the cytotoxicity experiment. Fibroblasts were seeded with the density of 4 x 10^4/well in 24 well plates. After 1 day, serum starvation was performed for 2 hr, and then cells were incubated with riboflavin (0.1 μM~10 mM), GHK-Cu (0.1 μM~1 mM), and YC7 (0.1 μM~1 mM) dissolved medium for 24 hr at 37 ℃. MTT assay was performed to measure cell viability. Short term and long term proliferation tests of fibroblasts were performed by seeding the cells (1 x 10^4/well) in 24 well plates after making the hydrogels inside the wells. Short term proliferation was measured by MTT assay after 3 days incubation under serum

starvation, and long term proliferation was also measured by MTT assay at designated time points (3, 7, 14, 21, and 31 days). Hydrogel with no cell incubation was also put under same conditions to calculate corrected values.

2.6. *In vivo* Wound Healing Experiments

The animal study has been approved by the animal care and use committee of Korea Institute of Science and Technology and all handling of mice were performed in accordance with the institutional regulations. C57BL/6 mice (male, 5 weeks of age: Orient Bio Inc. Korea) were used in the wound healing model. The animals were housed five animals per cage prior to surgery, and acclimated to their environment for at least 1 week prior to the procedure. Animals were individually anaesthetized with intraperitoneal injection of 0.5% pentobarbital sodium (0.01 mL/g). The dorsal surface was shaved with an electric clipper followed by a depilatory agent to remove any remaining hair. A sterile 6 mm punch biopsy tool was used to create two wounds, one on each side of midline. HA-Ty hydrogel with no peptide or HA-Ty hydrogel with YC7 crosslinked together, was applied to the right hand side wound and covered up with an occlusive dressing (3M^{TM} Tegaderm^{TM}). Wounds were observed without removing the dressings until tissue exudates interfered with the visuals. For the histological analysis, half of the skin tissues of

sacrificed mice were collected at day 7 and 28, and fixed in 10% formalin. The fixated samples were sent to KNOTUS Co. Ltd, and analyzed by using Masson's Trichrome staining.

3. Results and Discussion

3.1. Preparation of Tyramine-conjugated Hyaluronic Acid

Tyramine was conjugated to HA by standard carbodiimide/active ester-mediated coupling reaction (Fig. 19). The degree of loading (number of tyramine molecules per 100 repeating units of HA) was calculated from 1H NMR data by comparing relative ratios of the peaks of the methyl protons of HA (1.9 ppm) and the phenyl protons of tyramine (7.2 and 6.9 ppm) (Fig. 20A). The degree of loading was controlled not to exceed 11 tyramine molecules per 100 HA units, because higher tyramine loading decreased the solubility of HA-Ty. The loading was easily controlled the adding equivalent amount of tyramine hydrochloride. The presence of tyramine on HA can be recognized by UV spectroscopy, because tyramine exhibits a unique absorbance peak at 274 nm (Fig. 20B). By comparing the UV absorbance of HA and tyramine-conjugated HA, it was affirmed that tyramine was well conjugated.

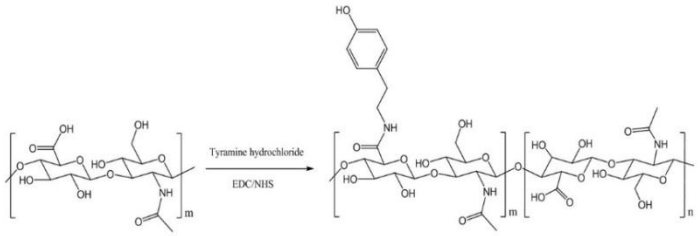

Tyramine · HCl equivalence	1 eq	2 eq	**3 eq**	6 eq
No. of Tyramines per 100 HA units	2~3	6~7	**9~11**	15~16

Figure 19. Tyramine conjugation to carboxylic acid of hyaluronic acid. Tyramine hydrochloride was conjugated via EDC/NHS coupling (top), and the number of tyramines per 100 HA units was controlled by the added equivalence of tyramine hydrochloride (bottom).

A

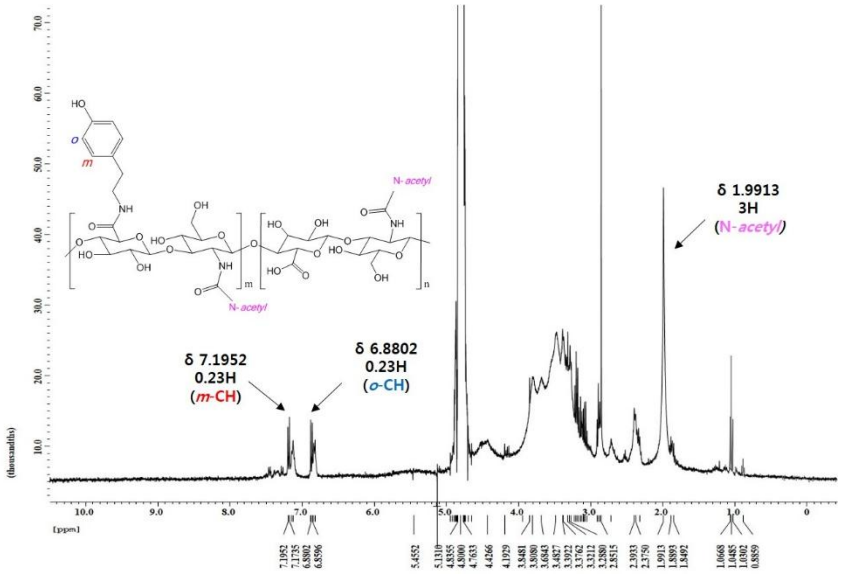

B

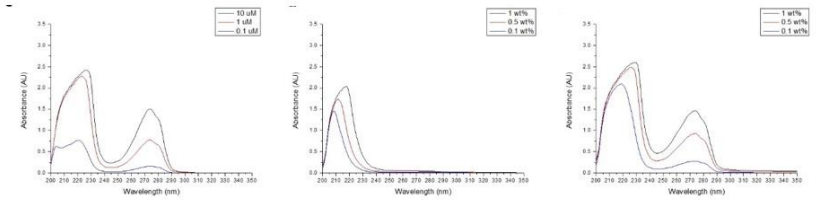

Figure 20. Characterization of HA-Ty. (A) 1H NMR spectra of HA-Ty. (B) UV absorption spectra of tyramine hydrochloride (left), pure HA (middle), and HA-Ty (right).

3.2. Optimization of Hydrogel Fabrication using Riboflavin and UVA

HA-Ty solution (1 wt%) was prepared in pH 7.4 PBS, which could be crosslinked by riboflavin and 365 nm UVA irradiation. Figure 21A shows the schematic formation of the crosslinked HA-Ty linked by the phenol moeities. The concentration of riboflavin was optimized first using the tilt test (Fig. 21B). Concentrations varying from 0.1 mg/mL to 20 mg/mL were used, where 20 mg/mL was the highest possible amount before saturation of riboflavin. The tilt test showed that 0.1 mg/mL and 20 mg/mL was not suitable for the gelation of HA-Ty. 1 mg/mL, 5 mg/mL, and 10 mg/mL all seemed acceptable for the gelation of HA-Ty according to the tilt test. However, only HA-Ty hydrogel made with 1 mg/mL concentration was easy to handle as a whole material and the designated concentration was used as the optimized gelling condition.

A

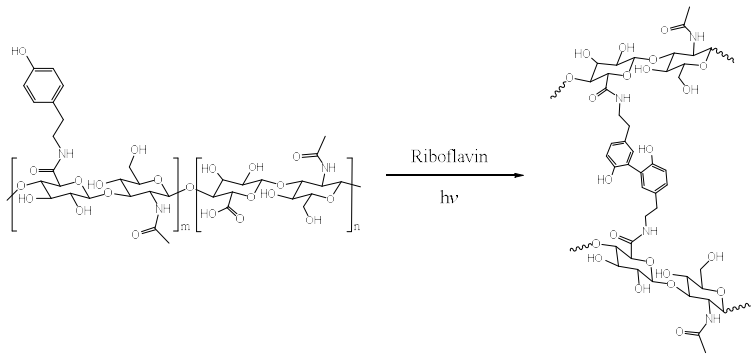

B

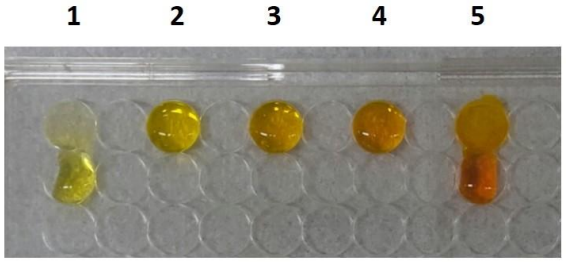

1 : 0.1 mg/mL 2 : 1 mg/mL 3 : 5 mg/mL
4 : 10 mg/mL 5 : 20 mg/mL

Figure 21. (A) Scheme of the gelation process of HA-Ty by riboflavin and UVA irradiation. (B) Tilt test of HA-Ty hydrogels made by different riboflavin concentrations.

3.3. Preparation of HA-Ty/TRP Hydrogel

The following TRPs were chosen for the crosslinking with HA-Ty; YYACAYY (YC7), dimerized YYACAYY (DYC7), YYAHAYY (YH7), YYAYY (YA5), and YYCYY (YC5). YC7 was chosen as a representative peptide because it showed a rapid self-assembling features in the previous study,[80] and the rests were selected due to their similarities in sequence compositions. Given the fact that phenol moieties can crosslink through a C-C linkage between ortho-carbons,[81] the crosslinked configuration of HA-Ty and TRPs could be illustrated as Scheme 3. To verify the crosslinking process of HA-Ty and TRPs by UV in the presence of riboflavin, time-dependent absorbance change was monitored during gelation. While non-crosslinked HA-Ty only showed an absorbance at 274 nm, new absorbance at 259 nm appeared, indicating that crosslinking between phenolic moieties occurred, which was further confirmed by a supplementary crosslinking test of tyramine hydrochloride solution.

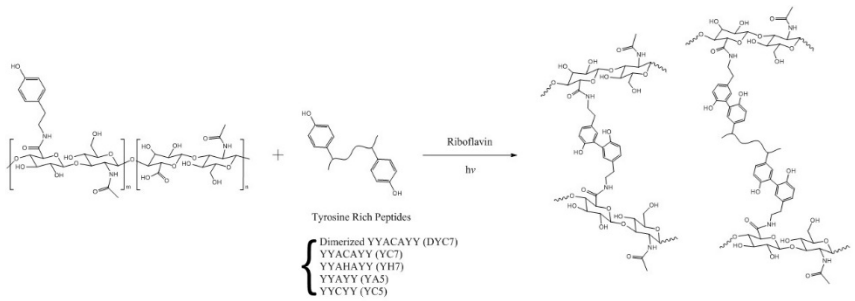

Scheme 3. Photo-crosslinked gelation of HA-Ty with the addition of different TRPs (DYC7, YC7, YH7, YA5, YC5).

3.4. Characterization of HA-Ty/TRP Hydrogel

First, gelation time was observed by rheometric measurement (Fig. 22). While the majority of TRP mixed hydrogels showed similar gelation time around 50~100 seconds, YC7 demonstrated a delayed 200 seconds gelation time. This could indicate that time consuming event occurred when YC7 was crosslinking with HA-Ty. It is well known that crosslinking density is closely related to the mechanical properties of hydrogels.[82] The storage modulus (G') is a reliable standard to know how rigid the subjected hydrogel is. The G' of HA-Ty hydrogel without any peptide addition was 156.6 Pa at a strain of 1% at 30 rad/s (Fig. 23B). The addition of TRPs increased the G', indicating that the peptides were able to strengthen the hydrogel by increasing the crosslinking densities. The G' of DYC7 (297.6 Pa) and YC7 (271.8 Pa) are the two highest cases, which are almost twice as that of the HA-Ty hydrogel. Interestingly, YH7 peptide which has only one amino acid difference from YC7 showed almost the same G' as HA-Ty at 30 rad/s. YH7 is specifically designed to

coordinate with metal ions to form nanoparticles,[83] but it is just a hydrophilic peptide without metals. This indicates that the crosslinking degree of HA-Ty is not dependent on the TRP's length, but the sequence itself. This coincides with the result of YA5 and YC5, where the G' of these two cases were higher than YH7 even though they are shorter in length.

This propensity was also observed by the swelling properties of the hydrogels (Fig. 24A). Swelling behavior of hydrogel is another indicator of the crosslinking density, which is inversely related to the rheological measurements. As expected, YC7 showed the least swelling ratio (206.6) compared to HA-Ty alone (674. 6). Coinciding results were observed with the degradation tests, where DYC7 and YC7 showed the latest degradation rate (Fig. 24B). Considering the solubility problem of DYC7, YC7 seemed to be the most suitable for the modulation of HA-Ty hydrogel.

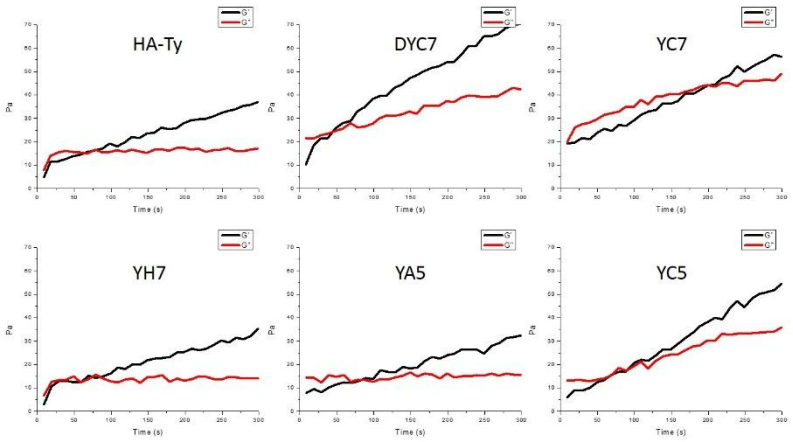

Figure 22. Gelation time of HA-Ty hydrogels using various TRPs (DYC7, YC7, YH7, YA5, YC5).

A

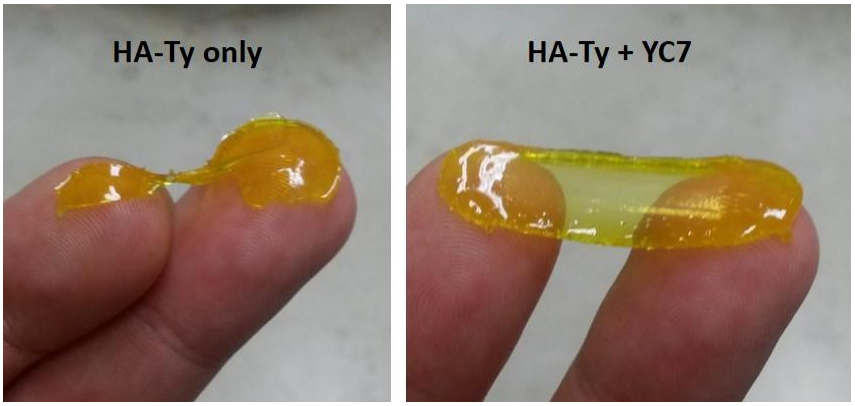

B

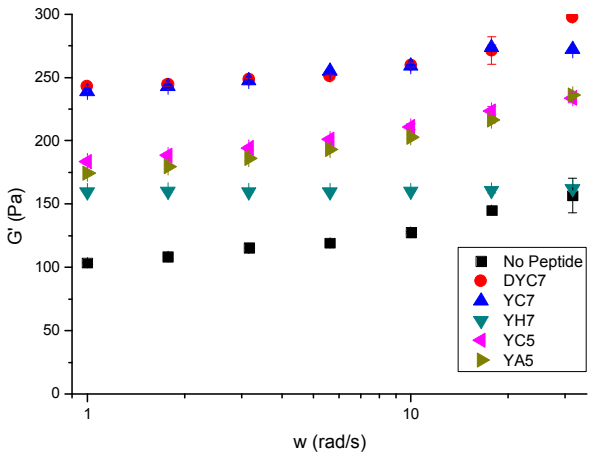

Figure 23. (A) Optical image of HA-Ty and HA-Ty/YC7 hydrogels. (B) Storage modulus of HA-Ty hydrogels made with different TRPs (DYC7, YC7, YH7, YC5, YA5).

A

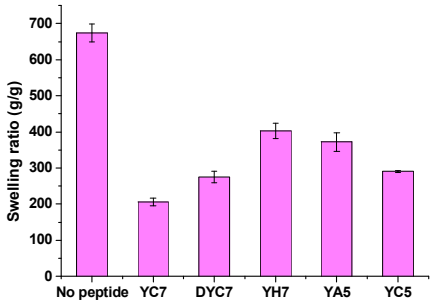

B

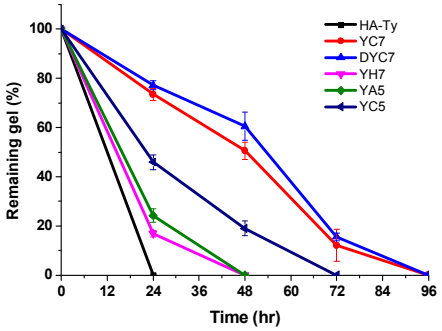

Figure 24. (A) Swelling and (B) degradation properties of HA-Ty hydrogels with different TRPs (YC7, DCY7, YH7, YA5, YC5).

3.4. Proliferation Test using Human Dermal Fibroblasts and Mesenchymal Stem Cells

GHK-Cu was used as an additive to enhance the wound healing functionality of the hydrogel. To evaluate the wound healing potential of the GHK-Cu incorporated hydrogel, proliferation test was performed using human dermal fibroblast and mesenchymal stem cells. Cytotoxicity of the hydrogel components was observed on both cell lines, where riboflavin, GHK-Cu, and YC7 showed no toxic events regardless of its concentration (Fig. 25). Overall, 1 wt% HA-Ty, 0.1 mM GHK-Cu, and 0.1 mM YC7 were mixed in PBS (1% DMSO), crosslinked by UVA in the presence of riboflavin, and the resulting hydrogel was subjected to the proliferation test. Short term (3 days incubation) examination showed that HA-Ty hydrogel itself could enhance the growth of fibroblasts more than four times than the control, and the addition of GHK-Cu extended this effect up to almost seven fold (Fig. 26A). Similar propensity was shown in the case with mesenchymal stem cells, in which the hydrogel environment enhanced the growth up to

five times, and GHK-Cu provided more than six times greater proliferation (Fig. 26B). This clearly showed that the HA-Ty hydrogel could be used an effective wound healing agent, especially with the aid of GHK-Cu.

A

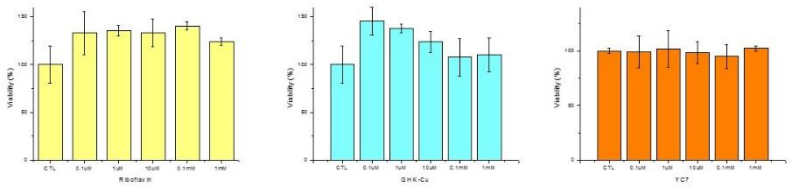

B

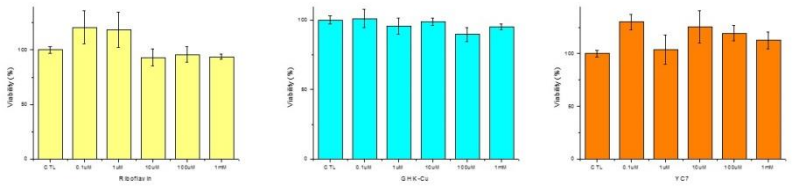

Figure 25. Cytotoxicity test of hydrogel components. (A) Viability of human dermal fibroblast against riboflavin, GHK-Cu, and YC7. (B) Viability of mesenchymal stem cells against riboflavin, GHK-Cu, and YC7.

A

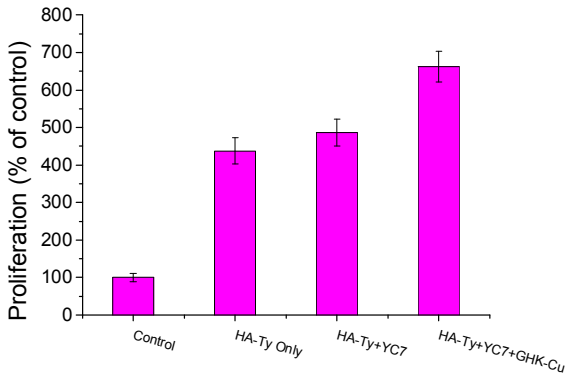

B

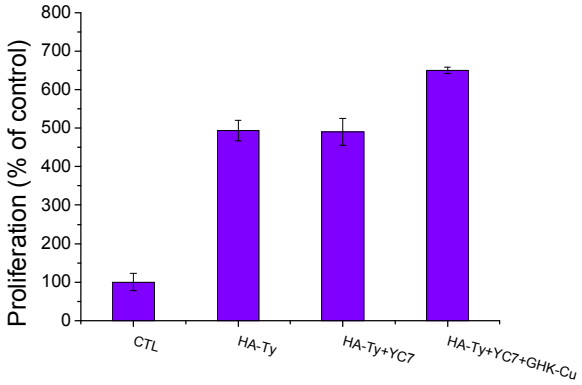

Figure 26. 3-day proliferation test using HA-Ty, HA-Ty/YC7, HA-Ty/YC7/GHK-Cu hydrogels. (A) Proliferation of human dermal fibroblasts after 3-day incubation in hydrogels. (B) Proliferation of mesenchymal stem cells after 3-day incubation in hydrogels.

3.5 Effects of HA-Ty/YC7 Hydrogel in Wound Healing Applications

To evaluate the wound healing effects of HA-Ty/YC7 hydrogel, several experiments were performed with human cell line and mice. Human dermal fibroblast was used first to perform the scratch assay. Scratch assay is a convenient method to observe cell migration *in vitro* [84]. An artificial gap is made by scratching on a confluent cell monolayer, and closing of the gap by cell migration is observed. Since direct contact of the hydrogel on cell monolayers could disrupt the environment, Transwell® system was applied so that the hydrogel placed in the upper filter could indirectly affect the cells.

As shown in figure 27, gap closure was observed 3 days after treating HA-Ty and HA-Ty/YC7 hydrogels on the scratched fibroblast monolayer, and both cases showed enhanced cell migration compared to control. When HA-Ty and HA-Ty/YC7 was compared, HA-Ty showed slightly more enhanced cell migration than HA-Ty/YC7. This is most likely because of the

faster degradation of HA-Ty, and the degraded HA would have affected the growth of fibroblasts in an earlier stage than HA-Ty/YC7. With just the cell migration results, faster degradation of the hydrogel seemed more advantageous.

However, the results were other way around in the case of wound healing experiments *in vivo*. The photographs of the healing process in mouse wound model showed enhanced wound healing effects by HA-Ty/YC7 while 3M™ Tegaderm™ was used as control (Fig. 28A). This coincides with the wound closure curve of the wound healing process where the healing effect is boosted at 14 days by HA-Ty/YC7 (Fig. 28B). This phenomenon could be explained by the difference in swelling and degradation of the hydrogels. As demonstrated in the *in vitro* experiments, HA-Ty/YC7 hydrogel swells less and degrades slower than HA-Ty hydrogel. This was also observed during the healing process, where HA-Ty began to swell in the early stage of 3 days. On day 7, HA-Ty/YC7 is still transparent, whereas HA-Ty is even more swollen and also opaque (Fig. 28C). It could be assumed that delayed swelling and

degradation of the HA-Ty/YC7 hydrogel led to better wound healing, because the monomerized HA units were not wasted. HA-Ty/YC7 was better maintained than HA-Ty by the Tegaderm^{TM} throughout the process contributing to the healing mechanism. This was also further analyzed by the Masson's Trichrome staining, where Tegaderm^{TM} was not able to prevent heavy inflammation even on day 28 (Fig. 29). HA-Ty and HA-Ty/YC7 showed relatively enhanced recovery of the wounds, where HA-Ty/YC7 performed better wound closure at the epithelial layer.

A

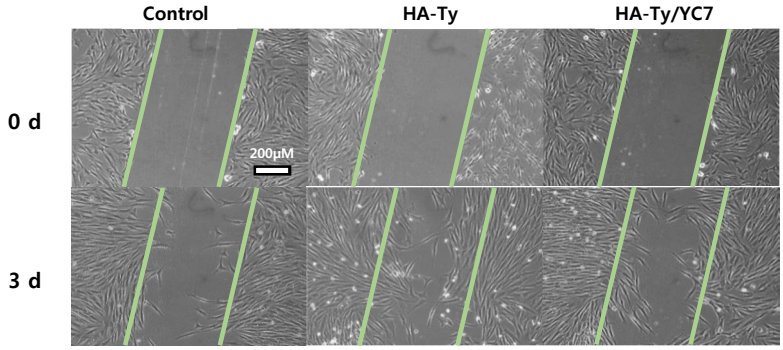

B

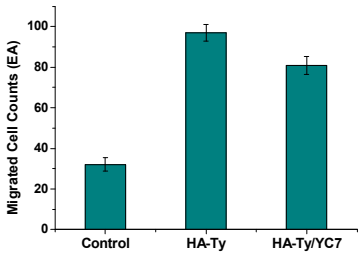

Figure 27. Analysis of human dermal fibroblast migration by in vitro scratch assay. (a) Images acquired on day 0 and 3 for control, HA-Ty treated culture, and HA-Ty/YC7 treated culture. Equivalent scratches were made by sterile pipette tips and each hydrogel sample was applied using Transwell® inserts. (b) Cell counts of migrated dermal fibroblasts within the colored boundary on day 3.

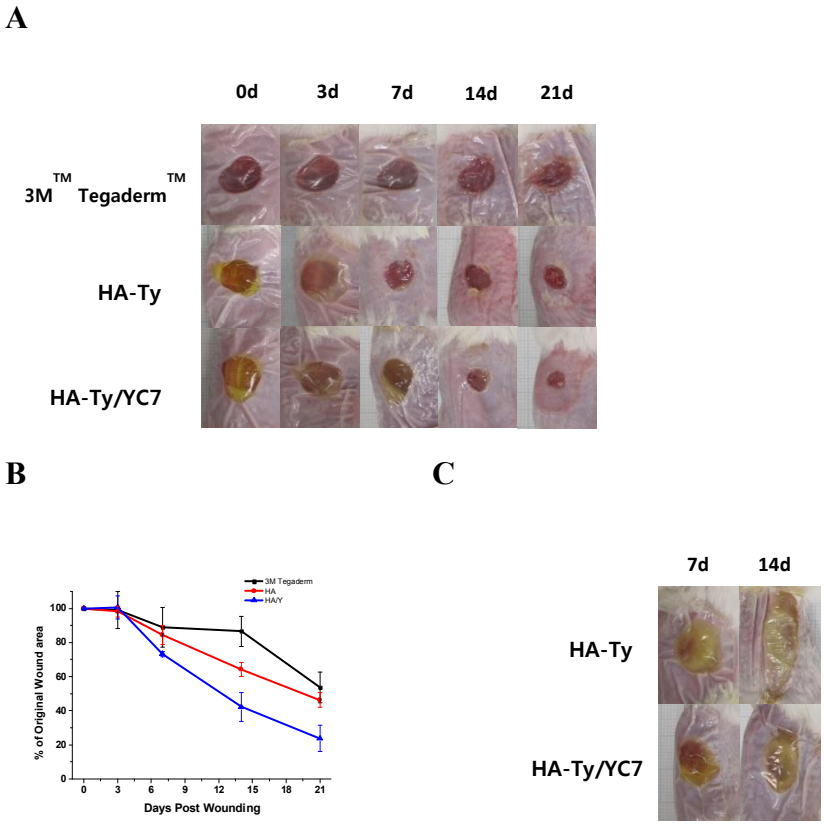

Figure 28. Effects of HA hydrogel and HA/YC7 hydrogel applied to open wound. (a) Photographs of wound healing process. (b) Wound closure curves demonstrate accelerated healing with HA/YC7 hydrogel compared to HA hydrogel. (c) Swelling and degradation progress of HA-Ty and HA-Ty/YC7 hydrogels.

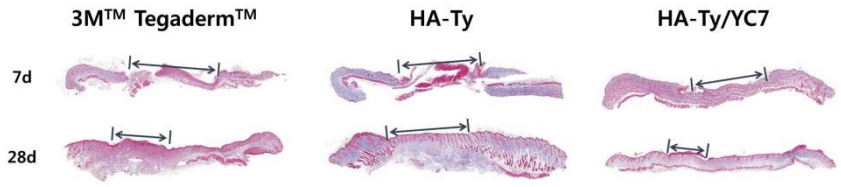

Figure 29. Masson′s Trichrome staining of open wounds treated by 3M™ Tegaderm™, HA hydrogel and HA/YC7 hydrogel on day 7 and 28. Wound gaps (arrows) showed accelerated healing of the epithelial layer with HA/YC7 hydrogel compared to HA hydrogel.

4. Conclusion

In conclusion, HA-Ty based hydrogel by UV crosslinking was prepared in the presence of riboflavin as a photo-initiator. Modulation of the hydrogel's properties was possible by adding TRPs in the crosslinking process, which changed the storage modulus (G') and swelling/degradation ratios of the hydrogel. Comparing five different TRPs, YC7 proved to be the most pertinent peptide to impart proper characteristics for further applications. YC7 effectively enhanced the crosslinking density of HA-Ty hydrogel. The hydrogel also demonstrated improved proliferation property on human dermal fibroblasts, together with GHK-Cu, which could provide synergistic effects on the wound healing. Even without the aid of GHK-Cu, HA-Ty/YC7 hydrogel successfully enhanced the healing process in the mouse wound model because of the hydrogel's delayed degrading properties. The riboflavin-induced HA-Ty based hydrogel is promising as a new biomaterial, which showed excellent results in wound healing applications.

Appendix

Ppa-ConC-BK01

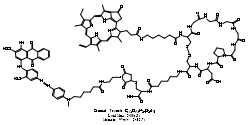

MALDI-TOF on CHCA matrix m/z calcd. for C112H135N24O27S5

(Ppa-ConC-BK01, [M+H]) 2407.8532, found 2407.5589.

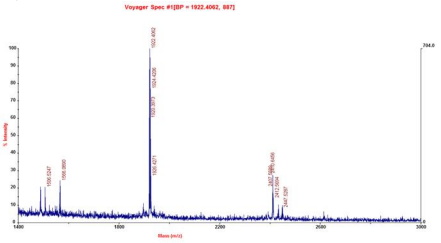

Ppa-iRGDC

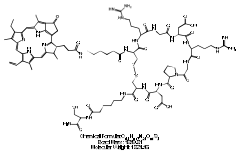

MALDI-TOF on CHCA matrix m/z calcd. for C83H118N23O18S3 (PPa-iRGDC, [M+H])

1820.8187, found 1821.3630.

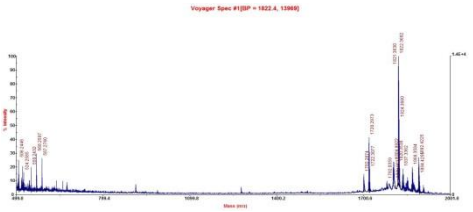

Ppa-iRGDC-BK01

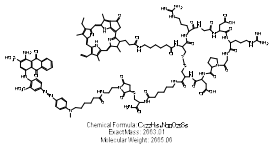

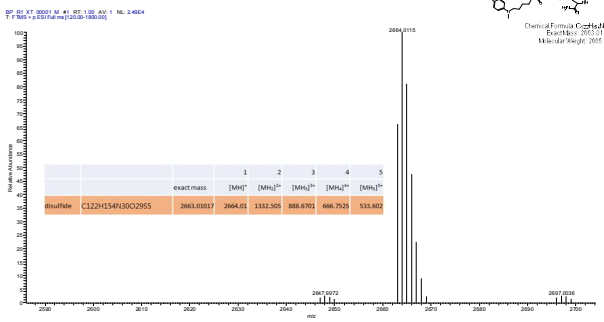

		exact mass	1 $[MH]^+$	2 $[MH_2]^{2+}$	3 $[MH_3]^{3+}$	4 $[MH_4]^{4+}$	5 $[MH_5]^{5+}$
disulfide	C122H154N30O29S5	2663.01017	2664.01	1332.505	888.6701	666.7525	533.602

mRNA analysis of HDF using Next Generation Sequencing (NGS)

Number of genes	Oligo HA	GHK-Cu	Oligo HA + GHK-Cu
Up-regulated	78	139	119
Down-regulated	246	239	259
Total	324	378	378

- Total of 19869 genes in Human Dermal Fibroblasts.
- Number of genes changed are written in table compared to control HDF.

Gene classification & Functional annotation clustering analysis

Control vs Oligo

	Gene Group 1	Enrichment Score: 0.39 RG	
1	11141	interleukin 1 receptor accessory protein like 1 (IL1RAPL1)	
2	10326	signal regulatory protein beta 1(SIRPB1)	
3	9214	Fc fragment of IgM receptor(FCMR)	
4	29802	pre-B lymphocyte 3(VPREB3)	

Gene classification & Functional annotation clustering analysis

Control vs GHK-Cu

	Gene Group 1	Enrichment Score: 0.97	RG
1	140686	WAP four-disulfide core domain 3(WFDC3)	
2	9068	angiopoietin like 1(ANGPTL1)	
3	10068	interleukin 18 binding protein(IL18BP)	
4	1474	cystatin E/M(CST6)	
	Gene Group 2	**Enrichment Score: 0.12**	**RG**
1	339456	transmembrane protein 52(TMEM52)	
2	219738	chromosome 10 open reading frame 35(C10orf35)	
3	161247	fat storage inducing transmembrane protein 1(FITM1)	
4	92270	ATPase H+ transporting accessory protein 1 like (ATP6AP1L)	
5	284021	mast cell immunoglobulin like receptor 1(MILR1)	
6	340393	transmembrane protein 249(TMEM249)	
7	196500	PILR alpha associated neural protein(PIANP)	
8	91319	derlin 3(DERL3)	
9	388799	family with sequence similarity 209 member B (FAM209B)	
10	2859	G protein-coupled receptor 35(GPR35)	
11	388588	small integral membrane protein 1 (Vel blood group) (SMIM1)	
12	728229	transmembrane protein 191B(TMEM191B)	
13	28959	transmembrane protein 176B(TMEM176B)	
14	92162	transmembrane protein 88(TMEM88)	
15	64102	tenomodulin(TNMD)	

Control vs Oligo HA + GHK-Cu

	Gene Group 1	Enrichment Score: 0.71	RG
1	353345	G protein-coupled receptor 141(GPR141)	
2	5791	protein tyrosine phosphatase, receptor type E (PTPRE)	
3	56113	protocadherin gamma subfamily A, 2(PCDHGA2)	
4	340393	transmembrane protein 249(TMEM249)	
5	107987545	olfactory receptor 2A7(LOC107987545)	
6	259294	taste 2 receptor member 19(TAS2R19)	
7	56112	protocadherin gamma subfamily A, 3(PCDHGA3)	
8	56111	protocadherin gamma subfamily A, 4(PCDHGA4)	
9	163590	torsin 1A interacting protein 2(TOR1AIP2)	
10	144245	ALG10B, alpha-1,2-glucosyltransferase(ALG10B)	
11	64102	tenomodulin(TNMD)	
	Gene Group 2	**Enrichment Score: 0.4**	**RG**
1	7710	zinc finger protein 154(ZNF154)	
2	147660	zinc finger protein 578(ZNF578)	
3	65243	ZFP69 zinc finger protein B(ZFP69B)	
4	100381270	zinc finger BED-type containing 6(ZBED6)	

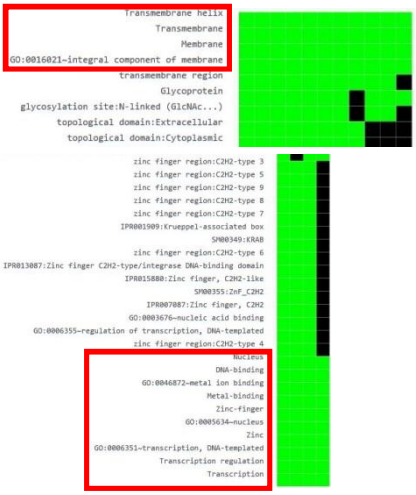

corresponding gene-term association not reported yet

Upregulated genes related pathway based on KEGG database

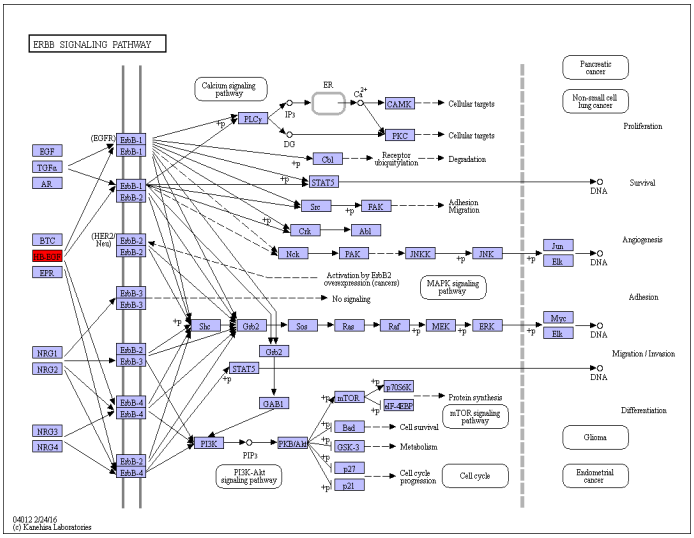

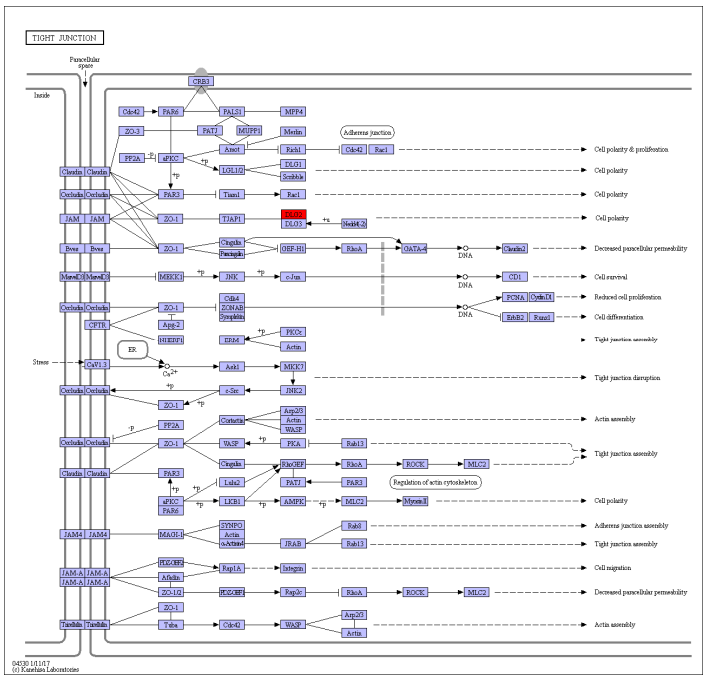

References

1 Chen, X. Y., Zaro, J. L. & Shen, W. C. Fusion protein linkers: Property, design and functionality. *Adv Drug Deliver Rev* **65**, 1357-1369, doi:10.1016/j.addr.2012.09.039 (2013).

2 Gokhale, R. S. & Khosla, C. Role of linkers in communication between protein modules. *Current opinion in chemical biology* **4**, 22-27 (2000).

3 Ikebe, M. *et al.* A hinge at the central helix of the regulatory light chain of myosin is critical for phosphorylation-dependent regulation of smooth muscle myosin motor activity. *J Biol Chem* **273**, 17702-17707 (1998).

4 Argos, P. An investigation of oligopeptides linking domains in protein tertiary structures and possible candidates for general gene fusion. *J Mol Biol* **211**, 943-958 (1990).

5 Amet, N., Lee, H.-F. & Shen, W.-C. Insertion of the designed helical linker led to increased expression of tf-based fusion proteins. *Pharmaceutical research* **26**, 523 (2009).

6 George, R. A. & Heringa, J. An analysis of protein domain linkers: their classification and role in protein folding. *Protein Engineering, Design and Selection* **15**, 871-879 (2002).

7 Chen, X., Bai, Y., Zaro, J. L. & Shen, W.-C. Design of an in vivo cleavable disulfide linker in

recombinant fusion proteins. *Biotechniques* **49**, 513 (2010).

8 Thorpe, P. E. *et al.* New coupling agents for the synthesis of immunotoxins containing a hindered disulfide bond with improved stability in vivo. *Cancer Res* **47**, 5924-5931 (1987).

9 Mason, S. D. & Joyce, J. A. Proteolytic networks in cancer. *Trends Cell Biol* **21**, 228-237, doi:10.1016/j.tcb.2010.12.002 (2011).

10 Busti, C., Falcinelli, E., Momi, S. & Gresele, P. Matrix metalloproteinases and peripheral arterial disease. *Internal and emergency medicine* **5**, 13-25 (2010).

11 Herszényi, L., Hritz, I., Lakatos, G., Varga, M. Z. & Tulassay, Z. The behavior of matrix metalloproteinases and their inhibitors in colorectal cancer. *Int J Mol Sci* **13**, 13240-13263 (2012).

12 Sapna, G., Gokul, S. & Bagri-Manjrekar, K. Matrix metalloproteinases and periodontal diseases. *Oral diseases* **20**, 538-550 (2014).

13 Li, H. *et al.* A systematic review of matrix metalloproteinase 9 as a biomarker of survival in patients with osteosarcoma. *Tumor Biology* **35**, 5487-5491 (2014).

14 Malemud, C. J. Matrix metalloproteinases (MMPs) in health and disease: an overview. *Frontiers in bioscience: a journal and virtual library* **11**, 1696-1701 (2006).

15 Li, S.-Y. *et al.* Protease-activable cell-penetrating peptide-protoporphyrin conjugate for targeted photodynamic therapy in vivo. *ACS applied materials & interfaces* **7**, 28319-28329 (2015).
16 Cohen, G. M. Caspases: the executioners of apoptosis. *Biochem J* **326**, 1-16 (1997).
17 Budihardjo, I., Oliver, H., Lutter, M., Luo, X. & Wang, X. Biochemical pathways of caspase activation during apoptosis. *Annual review of cell and developmental biology* **15**, 269-290 (1999).
18 Porter, A. G. & Jänicke, R. U. Emerging roles of caspase-3 in apoptosis. *Cell death & differentiation* **6** (1999).
19 Bullok, K. & Piwnica-Worms, D. Synthesis and characterization of a small, membrane-permeant, caspase-activatable far-red fluorescent peptide for imaging apoptosis. *J Med Chem* **48**, 5404-5407 (2005).
20 Yu, L. & Ding, J. Injectable hydrogels as unique biomedical materials. *Chem Soc Rev* **37**, 1473-1481 (2008).
21 Luo, Y., Kirker, K. R. & Prestwich, G. D. Cross-linked hyaluronic acid hydrogel films: new biomaterials for drug delivery. *J Control Release* **69**, 169-184 (2000).
22 Aimetti, A. A., Machen, A. J. & Anseth, K. S. Poly (ethylene glycol) hydrogels formed by

thiol-ene photopolymerization for enzyme-responsive protein delivery. *Biomaterials* **30**, 6048-6054 (2009).

23 Bahney, C. S., Hsu, C.-W., Yoo, J. U., West, J. L. & Johnstone, B. A bioresponsive hydrogel tuned to chondrogenesis of human mesenchymal stem cells. *The FASEB Journal* **25**, 1486-1496 (2011).

24 Kim, J. *et al.* Synthesis and characterization of matrix metalloprotease sensitive-low molecular weight hyaluronic acid based hydrogels. *Journal of Materials Science: Materials in Medicine* **19**, 3311-3318 (2008).

25 Tanihara, M., Suzuki, Y., Nishimura, Y., Suzuki, K. & Kakimaru, Y. Thrombin-sensitive peptide linkers for biological signal-responsive drug release systems. *Peptides* **19**, 421-425 (1998).

26 Dougherty, T. J. *et al.* Photodynamic therapy. *J Natl Cancer I* **90**, 889-905, doi:DOI 10.1093/jnci/90.12.889 (1998).

27 Dolmans, D. E. J. G. J., Fukumura, D. & Jain, R. K. Photodynamic therapy for cancer. *Nat Rev Cancer* **3**, 380-387, doi:10.1038/nrc1071 (2003).

28 Henderson, B. W. & Dougherty, T. J. How Does Photodynamic Therapy Work. *Photochem Photobiol* **55**, 145-157, doi:DOI 10.1111/j.1751-1097.1992.tb04222.x (1992).

29 MacDonald, I. J. & Dougherty, T. J. Basic principles of photodynamic therapy. *J Porphyr*

Phthalocya **5**, 105-129, doi:DOI 10.1002/jpp.328 (2001).

30 Brown, S. B., Brown, E. A. & Walker, I. The present and future role of photodynamic therapy in cancer treatment. *Lancet Oncol* **5**, 497-508, doi:Doi 10.1016/S1470-2045(04)01529-3 (2004).

31 Chatterjee, D. K., Fong, L. S. & Zhang, Y. Nanoparticles in photodynamic therapy: An emerging paradigm. *Adv Drug Deliver Rev* **60**, 1627-1637, doi:10.1016/j.addr.2008.08.003 (2008).

32 DeRosa, M. C. & Crutchley, R. J. Photosensitized singlet oxygen and its applications. *Coordin Chem Rev* **233**, 351-371, doi:Pii S0010-8545(02)00034-6
Doi 10.1016/S0010-8545(02)00034-6 (2002).

33 Verma, S., Watt, G. M., Mal, Z. & Hasan, T. Strategies for enhanced photodynamic therapy effects. *Photochem Photobiol* **83**, 996-1005, doi:10.1111/j.1751-1097.2007.00166.x (2007).

34 Clo, E., Snyder, J. W., Ogilby, P. R. & Gothelf, K. V. Control and selectivity of photosensitized singlet oxygen production: Challenges in complex biological systems. *Chembiochem* **8**, 475-481, doi:10.1002/cbic.200600454 (2007).

35 Zheng, G. *et al.* Photodynamic molecular beacon as an activatable photosensitizer based on protease-controlled singlet oxygen

quenching and activation. *P Natl Acad Sci USA* **104**, 8989-8994, doi:10.1073/pnas.0611142104 (2007).

36 Fisher, A. M. R., Murphree, A. L. & Gomer, C. J. Clinical and Preclinical Photodynamic Therapy. *Laser Surg Med* **17**, 2-31, doi:DOI 10.1002/lsm.1900170103 (1995).

37 Potter, W. R., Mang, T. S. & Dougherty, T. J. The Theory of Photodynamic Therapy Dosimetry - Consequences of Photodestruction of Sensitizer. *Photochem Photobiol* **46**, 97-101, doi:DOI 10.1111/j.1751-1097.1987.tb04741.x (1987).

38 Mang, T. S. *et al.* Photobleaching of Porphyrins Used in Photodynamic Therapy and Implications for Therapy. *Photochem Photobiol* **45**, 501-506, doi:DOI 10.1111/j.1751-1097.1987.tb05409.x (1987).

39 van Nostrum, C. F. Polymeric micelles to deliver photosensitizers for photodynamic therapy. *Adv Drug Deliver Rev* **56**, 9-16, doi:10.1016/j.addr.2003.07.013 (2004).

40 Lim, C. K. *et al.* Nanophotosensitizers toward advanced photodynamic therapy of Cancer. *Cancer Lett* **334**, 176-187, doi:10.1016/j.canlet.2012.09.012 (2013).

41 Sugahara, K. N. *et al.* Tissue-Penetrating Delivery of Compounds and Nanoparticles into Tumors. *Cancer Cell* **16**, 510-520,

doi:10.1016/j.ccr.2009.10.013 (2009).
42 Cho, H.-J. *et al.* Activatable iRGD-based peptide monolith: Targeting, internalization, and fluorescence activation for precise tumor imaging. *Journal of Controlled Release* **237**, 177-184, doi:http://dx.doi.org/10.1016/j.jconrel.2016.06.032 (2016).
43 Kelbauskas, L. & Dietel, W. Internalization of Aggregated Photosensitizers by Tumor Cells: Subcellular Time-resolved Fluorescence Spectroscopy on Derivatives of Pyropheophorbide-a Ethers and Chlorin e6 under Femtosecond One- and Two-photon Excitation¶. *Photochem Photobiol* **76**, 686-694, doi:10.1562/0031-8655(2002)0760686IOAPBT2.0.CO2 (2002).
44 Kraljic, I., Mohsni, S. E. & Arvis, M. A GENERAL METHOD FOR THE IDENTIFICATION OF PRIMARY REACTIONS IN SENSITIZED PHOTOOXIDATIONS*. *Photochem Photobiol* **27**, 531-537, doi:10.1111/j.1751-1097.1978.tb07642.x (1978).
45 Mosinger, J. & Mička, Z. Quantum yields of singlet oxygen of metal complexes of meso-tetrakis(sulphonatophenyl) porphine. *Journal of Photochemistry and Photobiology A: Chemistry* **107**, 77-82, doi:http://dx.doi.org/10.1016/S1010-

6030(96)04613-8 (1997).
46 Wu, H. *et al.* Imaging Integrin αvβ3 and NRP-1 Positive Gliomas with a Novel Fluorine-18 Labeled RGD-ATWLPPR Heterodimeric Peptide Probe. *Molecular Imaging and Biology* **16**, 781-792, doi:10.1007/s11307-014-0761-0 (2014).
47 Amiram, M., Luginbuhl, K. M., Li, X. H., Feinglos, M. N. & Chilkoti, A. Injectable protease-operated depots of glucagon-like peptide-1 provide extended and tunable glucose control. *P Natl Acad Sci USA* **110**, 2792-2797, doi:10.1073/pnas.1214518110 (2013).
48 Amiram, M., Luginbuhl, K. M., Li, X., Feinglos, M. N. & Chilkoti, A. A depot-forming glucagon-like peptide-1 fusion protein reduces blood glucose for five days with a single injection. *J Control Release* **172**, 144-151, doi:10.1016/j.jconrel.2013.07.021 (2013).
49 Bonnett, R. & Martinez, G. Photobleaching of sensitisers used in photodynamic therapy. *Tetrahedron* **57**, 9513-9547, doi:Doi 10.1016/S0040-4020(01)00952-8 (2001).
50 Boateng, J. S., Matthews, K. H., Stevens, H. N. E. & Eccleston, G. M. Wound healing dressings and drug delivery systems: A review. *J Pharm Sci-Us* **97**, 2892-2923, doi:10.1002/jps.21210 (2008).
51 Morgan, D. Wound management products in the drug tariff. *Pharmaceutical journal* **263**, 820-825

(1999).
52 Wiig, M. E. *et al.* The early effect of high molecular weight hyaluronan (hyaluronic acid) on anterior cruciate ligament healing: an experimental study in rabbits. *Journal of Orthopaedic Research* **8**, 425-434 (1990).
53 Weigel, P. H., Fuller, G. M. & LeBoeuf, R. D. A model for the role of hyaluronic acid and fibrin in the early events during the inflammatory response and wound healing. *Journal of theoretical biology* **119**, 219-234 (1986).
54 Davidson, J. M. *et al.* Hyaluronate derivatives and their application to wound healing: preliminary observations. *Clinical materials* **8**, 171-177 (1991).
55 Brown, J. The role of hyaluronic acid in wound healing's proliferative phase. *Journal of wound care* **13**, 48-51 (2004).
56 Ren, G., Dong, F., Wang, J. & Shi, P. The effect of hyaluronic acid external film on rats wound healing. *Zhonghua zheng xing wai ke za zhi= Zhonghua zhengxing waike zazhi= Chinese journal of plastic surgery* **20**, 380-383 (2004).
57 Depalma, R. L. *et al.* Characterization and quantitation of wound matrix in the fetal rabbit. *Matrix* **9**, 224-231 (1989).
58 Abatangelo, G., Martelli, M. & Vecchia, P. Healing of hyaluronic acid-enriched wounds: histological observations. *Journal of Surgical*

Research **35**, 410-416 (1983).

59 West, D. C., Hampson, I. N., Arnold, F. & Kumar, S. Angiogenesis induced by degradation products of hyaluronic acid. *Science* **228**, 1324-1327 (1985).

60 Park, H., Choi, B., Hu, J. & Lee, M. Injectable chitosan hyaluronic acid hydrogels for cartilage tissue engineering. *Acta biomaterialia* **9**, 4779-4786 (2013).

61 Kim, S.-h. & Chu, C.-C. Visible light induced dextran-methacrylate hydrogel formation using (−)-riboflavin vitamin B2 as a photoinitiator and L-arginine as a co-initiator. *Fibers and Polymers* **10**, 14-20 (2009).

62 Heo, J. *et al.* Riboflavin-induced photo-crosslinking of collagen hydrogel and its application in meniscus tissue engineering. *Drug delivery and translational research* **6**, 148-158 (2016).

63 Orlowska, M. *et al.* Continuous and pulsed ultraviolet light for nonthermal treatment of liquid foods. Part 1: effects on quality of fructose solution, apple juice, and milk. *Food and Bioprocess Technology* **6**, 1580-1592 (2013).

64 Correia, M., Neves-Petersen, M. T., Jeppesen, P. B., Gregersen, S. & Petersen, S. B. UV-light exposure of insulin: pharmaceutical implications upon covalent insulin dityrosine dimerization and disulphide bond photolysis. *Plos One* **7**,

e50733 (2012).
65 Kogan, G., Šoltés, L., Stern, R. & Gemeiner, P. Hyaluronic acid: a natural biopolymer with a broad range of biomedical and industrial applications. *Biotechnology letters* **29**, 17-25 (2007).
66 Collins, M. N. & Birkinshaw, C. Hyaluronic acid based scaffolds for tissue engineering—A review. *Carbohydrate polymers* **92**, 1262-1279 (2013).
67 Kurisawa, M., Chung, J. E., Yang, Y. Y., Gao, S. J. & Uyama, H. Injectable biodegradable hydrogels composed of hyaluronic acid-tyramine conjugates for drug delivery and tissue engineering. *Chem Commun*, 4312-4314 (2005).
68 Andley, U. P. & Chakrabarti, B. Role of singlet oxygen in the degradation of hyaluronic acid. *Biochem Bioph Res Co* **115**, 894-901 (1983).
69 Greenwald, R. A. & Moy, W. W. Effect of oxygen-derived free radicals on hyaluronic acid. *Arthritis & Rheumatology* **23**, 455-463 (1980).
70 Elvin, C. M. *et al.* Synthesis and properties of crosslinked recombinant pro-resilin. *Nature* **437**, 999-1002, doi:10.1038/nature04085 (2005).
71 Jang, H.-S. *et al.* Tyrosine-mediated two-dimensional peptide assembly and its role as a bio-inspired catalytic scaffold. *Nat Commun* **5**, 3665 (2014).
72 Pickart, L., Vasquez-Soltero, J. M. & Margolina,

A. GHK peptide as a natural modulator of multiple cellular pathways in skin regeneration. *BioMed research international* **2015** (2015).

73 Pickart, L. The human tri-peptide GHK and tissue remodeling. *Journal of Biomaterials Science, Polymer Edition* **19**, 969-988 (2008).

74 Kang, Y.-A. *et al.* Copper-GHK increases integrin expression and p63 positivity by keratinocytes. *Archives of dermatological research* **301**, 301-306 (2009).

75 Deed, R. *et al.* Early-response gene signalling is induced by angiogenic oligosaccharides of hyaluronan in endothelial cells. Inhibition by non-angiogenic, high-molecular-weight hyaluronan. *International journal of cancer* **71**, 251-256 (1997).

76 Lesley, J., Hascall, V. C., Tammi, M. & Hyman, R. Hyaluronan binding by cell surface CD44. *J Biol Chem* **275**, 26967-26975 (2000).

77 Slevin, M., Kumar, S. & Gaffney, J. Angiogenic oligosaccharides of hyaluronan induce multiple signaling pathways affecting vascular endothelial cell mitogenic and wound healing responses. *J Biol Chem* **277**, 41046-41059 (2002).

78 Dechert, T. A., Ducale, A. E., Ward, S. I. & Yager, D. R. Hyaluronan in human acute and chronic dermal wounds. *Wound Repair Regen* **14**, 252-258, doi:10.1111/j.1743-

6109.2006.00119.x (2006).
79 Rheinwald, J. G. & Green, H. Serial Cultivation of Strains of Human Epidermal Keratinocytes - Formation of Keratinizing Colonies from Single Cells. *Cell* **6**, 331-344, doi:Doi 10.1016/S0092-8674(75)80001-8 (1975).
80 (!!! INVALID CITATION !!! 49).
81 Musso, H. Phenol oxidation reactions. *Angewandte Chemie International Edition in English* **2**, 723-735 (1963).
82 Ifkovits, J. L. & Burdick, J. A. Review: photopolymerizable and degradable biomaterials for tissue engineering applications. *Tissue engineering* **13**, 2369-2385 (2007).
83 Kim, Y. O. *et al.* A tyrosine-rich peptide induced flower-like palladium nanostructure and its catalytic activity. *Rsc Adv* **5**, 78026-78029, doi:10.1039/c5ra11817d (2015).
84 Liang, C.-C., Park, A. Y. & Guan, J.-L. In vitro scratch assay: a convenient and inexpensive method for analysis of cell migration in vitro. *Nature protocols* **2**, 329-333 (2007).

요 약 (국문 초록)

펩타이드는 자연적으로 존재하고 생체 친화적이며 기능성을 보유하고 있는 물질로 다양한 생물의학적 연구에 활용되고 있다. 광범위하게 활용되고 있는 분야 중 하나는 암세포에 대한 약물 전달인데, 이때 RGD 혹은 MMP-7과 같이 암에 의한 과발현 인자에 관계된 펩타이드들이 활용된다. 최근에는 펩타이드의 구조적인 특성도 조명되고 있으며 이들은 하이드로젤과 같은 생체재료의 형성에 활용될 수 있다.

제 1 장에서는 암세포 침투가 가능한 iRGD 펩타이드로 Ppa-iRGDC-BK01이라는 물질을 디자인했다. Ppa-iRGDC-BK01은 스스로 응집하여 디포 (저장소)가 되는데 이를 암의 광역동 치료에 활용하고자 했다. 디포는 단백질 분해효소 및 환원성 분해에 의해 활성화가 가능한데 분해 전의 비활성 상태가 응집으로 인해서 소광 효과가 매우 뛰어난 것으로 확인됐다. 디포의 분해가 일어나면 Ppa는

펩타이드에 의해 암에 축적이 되는데 이 현상이 지속적으로 일어나며, 이로 인해 광감작 효과가 오래도록 유지될 수가 있다. 이와 같은 결과는 안전성이 뛰어나고 반복적인 광역동 치료를 단 한번의 물질 주입으로 가능하게 하여 암 치료에 있어서 새로운 지평을 열어줄 수 있을 것으로 기대된다.

제 2장에서는 티라민을 결합시킨 히알루론산 (HA-Ty)을 티로신이 풍부한 펩타이드 (TRP)를 이용하여 유체 물성이 변형된 하이드로젤을 만들었으며 이를 상처 치료제로 활용하고자 했다. 젤 형성 전략으로는 리보플라빈에 의한 광가교를 선택했으며, 리보플라빈은 자외선에 의해 페놀 그룹을 공유결합 시켜주는 역할을 한다. TRP는 히알루론산에 결합된 티라민에 가교가 될 수 있기에 하이드로젤의 저장 탄성률을 증가시키는 효과를 일으켰다. 최종적으로 형성된 HA-Ty/TRP 하이드로젤은 상처 치료에 활용될 수 있는 가능성을 보여줬다.

주요어 : 광역동 치료, 세포침투 RGD (iRGD), 활성화 광감작제, 피하주입 디포, 지속적인 물질 유입, 히알루론산 하이드로젤, 티로신이 풍부한 펩타이드, 리보플라빈, 광가교, 상처치료

학 번 : 2014-30250